Plasma Sources Science and Technology



# Coherent microwave scattering from resonance enhanced multi-photon ionization (Radar REMPI): A review

To cite this article before publication: Zhili Zhang *et al* 2021 *Plasma Sources Sci. Technol.* in press https://doi.org/10.1088/1361-6595/ac2350

# Coherent Microwave Scattering from Resonance Enhanced Multi-Photon Ionization (Radar REMPI): A Review

*Zhili Zhang[1], Mikhail N. Shneider[2], Richard B. Miles [2,3]*

[1]Mechanical, Aerospace and Biomedical Engineering, University of Tennessee, Knoxville TN 37996

[2]Mechanical and Aerospace Engineering, Princeton University, Princeton NJ 08544

[3]Aerospace Engineering, Texas A&M University, College Station, TX

## Abstract

Coherent microwave scattering from laser-induced plasmas, including weakly ionized plasma, laser sparks, Multiphoton Ionization (MPI), and Resonance Enhanced Multi-Photon Ionizations (Radar REMPI) has achieved much successes in plasma, reactive and nonreactive flow diagnostics. Under illumination of microwaves (Radar), electrons inside the laser-induced plasma oscillate with the electric field of the microwave and re-radiate from the electrons forming coherent scattering. In the far-field approximation, the microwave scattering from the small volume plasma reflects the generation and evolution of unbounded electrons inside the plasma, when the microwave wavelength is much greater than the size of the plasma and the skin layer depth at the microwave frequency is larger than the size of the plasma. Laser excitation schemes, microwave detection methods, calibration of microwave scattering, and the novel applications of the technique have been significantly expanded and improved. This review paper summarizes physical principles, various REMPI excitation schemes for atomic and molecular species, and temperature measurements in plasma and reactive flows. Discussions on new research directions and applications are given at the end.

**Key words**: Radar REMPI, microwave, combustion diagnostics, plasma diagnostics

# Table of Content

Coherent Microwave Scattering from Resonance Enhanced Multi-Photon Ionization (Radar REMPI): A Review ..... 1

Abstract ..... 1

Table of Content ..... 3

**1. Introduction and Background** ..... 4

**2. Coherent Microwave Scattering** ..... 7

**2.1 Theoretical consideration – Coherent Microwave Rayleigh scattering** ..... 7

**2.2 Experimental implementation of coherent microwave scattering** ..... 11

**2.3 Quantitative calibration of coherent microwave scattering** ..... 13

**3. Resonance-Enhanced Multiphoton Ionization (REMPI)** ..... 15

**3.1 Calculations of REMPI cross sections for atomic species** ..... 17

**3.2 Calculations of REMPI cross sections for molecular species** ..... 20

**4. Plasma Characterization by Coherent Microwave Scattering** ..... 22

**4.1 REMPI and Avalanche Plasma Modeling** ..... 22

**4.2 Experimental Plasma Measurements and Characterization** ..... 31

**5. Rotational Temperature Measurements** ..... 39

**6. Standoff Detection of Trace Species** ..... 46

**7. Conclusions and Outlook** ..... 48

**Acknowledgements** ..... 49

**References** ..... 50

## 1. Introduction and Background

Coherent microwave scattering from laser-induced plasmas has become an important quantitative diagnostic tool for measurements of electron number density, species concentrations, and temperature in plasma and non-reactive and reactive flows. The technique uses a laser to selectively generate ionization of a specific specie and coherent microwave scattering to sensitively and *in-situ* detect the evolution of electrons inside the ionization region. These features combine to offer a high-precision, quenching-robust ionization spectroscopy, which can not only perform partial functions of mass spectroscopy at any pressure, but also provide standoff detection capability.

In this approach, two physical processes occur. First a small-volume plasma or plasmas are generated by a focused laser beam. The plasmas can be either produced by laser-induced avalanche ionization (AI), Multiphoton Ionization (MPI), Resonance-Enhanced Multiphoton Ionization (REMPI), or tunneling ionization. In AI, a gaseous atom or molecule simultaneously absorbs multiple photons to be ionized. The seed electrons are then accelerated by the beam's electromagnetic field via the inverse Bremsstrahlung effect. If a sufficient field is applied, the electrons are accelerated to energies that cause electron impact ionization upon collisions with the neutral gas atoms and molecules. The newly liberated electrons then are accelerated by the field leading to an electron avalanche ionization (EAI) process during the laser pulse duration.[1]

Multiphoton Ionization (MPI), including Resonance-Enhanced Multiphoton Ionization (REMPI) occurs when multiple photons are simultaneously absorbed by an atom or molecule.[2] In REMPI, first m photons are simultaneously absorbed by the atom or molecule in the sample to bring it to an excited state. Other n photons are absorbed afterwards to generate an electron and ion pair. The so-called (m+n) REMPI is a nonlinear optical process, which can only occur within

the focus of the laser beam with sufficient high intensity. A small-volume plasma is thus formed near the laser focal region. If the energy of m photons does not match any state, an off-resonant transition can occur with an energy defect $\Delta E$, however, the electron is very unlikely to remain in that state. For large detuning, it resides there only during the time Δt. The uncertainty principle is satisfied for $\Delta t$, i.e., $\Delta E \cdot \Delta t \geq \hbar$, where $\hbar = h/2\pi$ and h is the Planck constant ($6.6261 \times 10^{-34}\, J \cdot s$). Such transition and states are called virtual, unlike real transitions to states with long lifetimes. The larger the energy defect is, the shorter the lifetime of the virtual transition is. The real transition probability is thus many orders of magnitude higher than the virtual transition one, which is called resonance enhanced effect.

Laser tunneling ionization [3] is a process in which electrons in an atom or molecule pass through the potential barrier to ionize the atom or molecule. It usually requires high optical intensity in ultrafast lasers to have the non-negligible Keldysh parameter, the ratio of the characteristic time that the electron takes to pass through the barrier formed by the electric field and static atomic potential to the cycle time of the oscillating electric field. An estimation of the Keldysh parameter is recommended for experiments and computations of using ultrafast laser to quantify the MPI and tunneling ionizations.

Second, under illumination of microwaves (Radar), electrons inside the plasma oscillate with the electric field of the microwave. [4] The re-radiation from the electrons forms coherent scattering, shown in Figure 1. When the microwave wavelength is much greater than the size of the plasma and the skin layer depth at the microwave frequency is larger than the size of the plasma, the plasma is transparent to the microwave field and thus all electrons inside oscillate in phase with the microwave. For 10 GHz microwave, skin layer thickness is about 2 mm for electrons at 1 part per million (ppm) or 200 μm for 10 ppm in atmospheric air. The skin layer thickness is same at

the same concentration for higher pressures. As a comparison, a typical laser-induced plasma for diagnostics is on the order of 10-100 μm in diameter. The conditions for coherent microwave scattering are satisfied for laser-induced plasmas at relatively low concentrations. In the far-field approximation, the microwave scattering from the small volume plasma lies in the Rayleigh range. The scattering signal reflects the generation and evolution of all unbounded electrons inside the plasma. For continuous wave microwave illumination, the plasma continues to scatter microwaves until the electrons have recombined or have attached to some other molecular species, producing the negative ions. The most important feature of the coherent Rayleigh scattering is that the electric field of the scattered microwave directly reflects the total electron number inside the plasma. The benefits of using microwave for detection include low power microwave, and low background and shot noise at microwave frequency and narrow bandwidth.

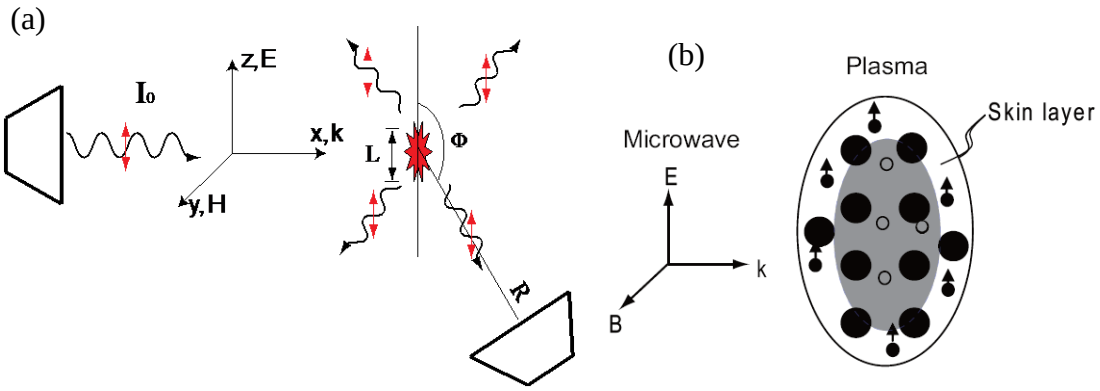


***Figure 1.*** *(a) Microwave scattering from a small volume plasma using double microwave horn antennas, with one horn for illumination and the other for detection. (b) The illustration of skin layer within the small volume plasma under microwave illumination. The current plot shows the skin layer thickness δ is less than the size of the plasma, resulting in the shielding effects for the electrons in the plasma.*

## 2. Coherent Microwave Scattering

### 2.1 Theoretical consideration – Coherent Microwave Rayleigh scattering

Plasma diagnostics with microwaves has been investigated for more than 40 years. Typical experimental and theoretical research has focused on plasmas, whose sizes are typically much larger than the microwave wavelength. Microwave transmission, reflection, interferometry, incoherent scattering, and microwave radiation from plasma were examined. [5, 6] However, when the size of a plasma is much smaller than microwave wavelength, the usual microwave measurement methods do not apply.[4]

A small-volume, non-stationary plasma can be produced by a focused, pulsed laser beam through avalanche ionization, REMPI, or tunneling ionization etc. The plasma located near the focal point of the laser beam is generally on the scale of tens of microns in diameter and less than a few millimeters in length. When it is illuminated by microwave whose wavelength is on the order of centimeters, the charge separation can be modulated, creating oscillating induced dipoles inside. The skin layer should be estimated, the skin layer thickness $\delta = 2/\sqrt{2\mu_0\sigma\omega_{mw}}$ at microwave frequency $\omega_{mw}$, plasma conductivity $\sigma$ and permeability $\mu_0$, is greater than the characteristic size of the plasma, all the electrons in the plasma oscillate in the same phase as the microwave. So, in the far field, the plasma can be regarded as one induced point dipole radiation source of microwaves, and the scattering falls into the Rayleigh scattering approximation. In that case, the scattered microwave power is directly proportional to the square of the number of electrons, which will be shown below. On the other hand, if the skin layer thickness $\delta$ is small, then some of the electrons are shielded as shown in Figure 1(b). In that case, the scattering falls into the Mie regime and no longer has a dipole character.[7] The Rayleigh regime is particularly interesting since in that regime, the microwave scattering intensity is directly related to the total

number of electrons and can be used for quantitative measurement of avalanche ionization and REMPI processes.

The physical process can be described as the following. An incident microwave of frequency $f_{mw} = \omega_{mw}/2\pi$ illuminate a small-volume plasma. The microwave penetrates and interacts with the weakly ionized plasma. Inside the plasma, electrons oscillate with the microwave while much heavier ions can be regarded as immobile. Mainly three forces act on the electrons: electron-neutral collisions, electron-ion attractions and electromagnetic force from microwave radiation. The volume of the plasma is considered to be small if the wavelength of the microwave is much larger than the size of the plasma. The field strength or intensity of the microwave can then be regarded as uniform across the spatial scale of the plasma. Within the skin layer δ at the microwave frequency $\omega_{MW}$, a partial differential equation for electron movement Δz can be written

$$\ddot{\Delta z} + \nu_m \dot{\Delta z} + \xi\omega_p^2 \Delta z = \frac{e}{m_e} E_o \cos(\omega_{mw} t) \quad (1)$$

where e is electron charge, $m_e$ is the mass of electron, $E_0$ is the electrical field of the microwave, $\omega_p = \sqrt{e^2 n_e/\varepsilon_0 m_e}$ is the electron plasma frequency and $\nu_m$ is the transport collisional frequency between electrons and neutrals. With an increased degree of ionization (usually, when $n_e/N_n > 10^{-3}$, $N_n$ is the density of neutral gas particles), instead of $\nu_{en}$, the full transport frequency $\nu_m = \nu_{en} + \sum_i \nu_{e+,i}$ must be taken into account, where $\sum_i \nu_{e+,i}$ is a summary frequency of Coulomb collisions with all sorts of positive ions. The frequency for electron-ion Coulomb collisions with ions of density $n_+$ is $\nu_{e+} \approx \frac{2.9\cdot 10^{-12} n_+ \ln\Lambda}{T_e^{3/2}}$ 1/sec ( $n_+$ - [$m^{-3}$], $T_e$ – [eV]), [8] where $\ln\Lambda = \ln\left(\frac{12\pi n_e \lambda_D^3}{Z}\right)$ is the Coulomb logarithm, Z is the charge of the ion (in most practical of practical range of conditions, Z=1); $\lambda_D = \left(\frac{\varepsilon_0 k T_e}{e^2 n_e^2}\right)^{1/2}$ the Debye length.

The microwave radiation can be of any polarization, but the strongest effect is when the microwave radiation is linearly polarized with its electric field $E_{MW}$ along the plasma column. The term $\xi\omega_p^2\Delta z$ in (1) is due to the weakening of the microwave field by polarized charges at the plasma boundaries. The factor $\xi$ in (1) depends on the considered plasma geometry and the direction of polarization of the scattered microwave field. Note that, in [4], equation (1) was obtained in the approximation of a homogeneous ion density in a cylindrical plasma in which the transverse dimensions are comparable with the longitudinal ones (along the polarization of the microwave field). In this case, $\xi$=1 is assumed. On the other hand, if, for example, the plasma has the shape of an elongated ellipsoid and the microwave polarization coincides with the direction of the larger axis of the ellipsoid, then $\xi$<<1 and the screening effect of the scattering charges at the plasma boundaries can be neglected.

Solving the equation of (1), assuming as in [4], $\xi$=1, in the far field approximation, where the distance between the receiver and the plasma is much greater than the microwave wavelength, which, in turn, is much greater than the scale of the plasma, the total intensity of coherently scattered microwave radiation averaged over a microwave cycle can be found as

$$\langle\Theta\rangle = \frac{I_m\omega_{mw}^4}{6\pi c^4\left[\left(\omega_p^2-\omega_{mw}^2\right)^2+\left(\nu_m\omega_{mw}\right)^2\right]}\frac{e^4{N_e}^2}{\varepsilon_0^2 m_e^2} \quad (2)$$

where $\langle\cdot\rangle$ means average over a microwave cycle, c is light speed in vacuum, $\varepsilon_0$ is the dielectric constant in vacuum, $I_m$ is the incident microwave intensity, $N_e$ is the total electron number in the plasma. In this case, the phase shift between the incident and scattered radiation [4]

$$\tan\varphi = -\nu_m\omega_{mw}/\left(\omega_p^2-\omega_{mw}^2\right) \quad (3)$$

which can be varied and even change sign during the space-time evolution of plasma. A phase shifter in the homodyne detection arm can be added for phase sensitive detection of the microwave signal, which can be used to distinguish the stray microwave from the signal.

In the collision dominated regime where $\nu_m \gg \omega_m, \omega_p$, the effective total "Rayleigh" scattering cross section can be written as

$$\sigma_R = \frac{\langle\Theta\rangle}{I_m} = \frac{e^4\omega_{mw}^4}{6\pi c^4 \varepsilon_0^2 m_e^2 \nu_m^2} {N_e}^2 \quad (4)$$

At $\nu_m \gg \omega_{mw} \gg \omega_p$, the equation (2) for scattered microwave intensity and scattered microwave electric field $E_{MW}$ can be approximately simplified as

$$\langle\Theta\rangle \approx I_i {N_e}^2 \omega_{mw}^2 \quad (5a)$$

$$\langle E_{MW}\rangle \approx E_i N \omega_m \quad (5b)$$

If The averaged power of microwave scattering is approximately proportional to the intensity of the incident microwave $I_i$, the square of the total electron number $N_e$ inside the plasma, and the square of the microwave frequency $\omega_{mw}$, , as shown in equation (5a). It should be noted that the averaged electric field of the microwave scattering is the square root of the averaged power. So, the averaged electric field of the microwave scattering is approximately proportional to the field of the incident microwave, the total number of the electrons inside the plasma, and the frequency of the microwave, as shown in equation (5b). It should be noted that $\nu_m$ might be unknown in certain situations, which requires to use equation (4) to interpret the microwave scattering.

## 2.2 Experimental implementation of coherent microwave scattering

The coherent microwave scattering system is generally based on homodyne or heterodyne technologies. These methods can significantly increase the detection sensitivity by suppressing the noise and follow sub-nanosecond plasma generation and evolution. The homodyne detection method mixes the detected microwave electric field with its own source to produce a signal proportional to the product of the two. The signal frequency is converted down from tens of gigahertz to below one gigahertz so that the signal can be amplified and observed with standard electronics devices. Heterodyne detection uses a separate microwave source to beat the microwave frequency down to an intermediate frequency range. Heterodyne detection is more suitable for broadcasting applications, where a single microwave source is not practical or may not be possible. Based on coherent detection theory, heterodyne detection power has a lower (3dB) Signal-to-Noise-Ratio (SNR) than homodyne detection, which is called the heterodyne penalty.[9] The origin of the heterodyne penalty is from the random phases in two microwave sources. Unless a phase-locked circuit between two microwave sources is used in heterodyne detection, homodyne detection always has a 3dB-better SNR.

Experimentally, a low power (~10dBm) microwave source (sweep oscillator, Gunn diode, and/or other microwave sources) can be applied and split into two channels. One channel is used to illuminate the ionization point through a microwave horn antenna. Microwave scattering from the plasma is collected by the same microwave horn and/or separate horns. The received microwave passes through a microwave circulator if using the same horn and is amplified >30 dB by one preamplifier at original microwave frequency. After the frequency is converted down in the mixer, two other amplifiers with lower bandwidth amplify the signal by another factor of ~60dB. From the geometry of dipole radiation, the polarization of the microwave must be chosen

to be along the propagation direction of the laser to maximize the scattering signal. The time-accurate microwave scattering signal is monitored and collected by an oscilloscope.

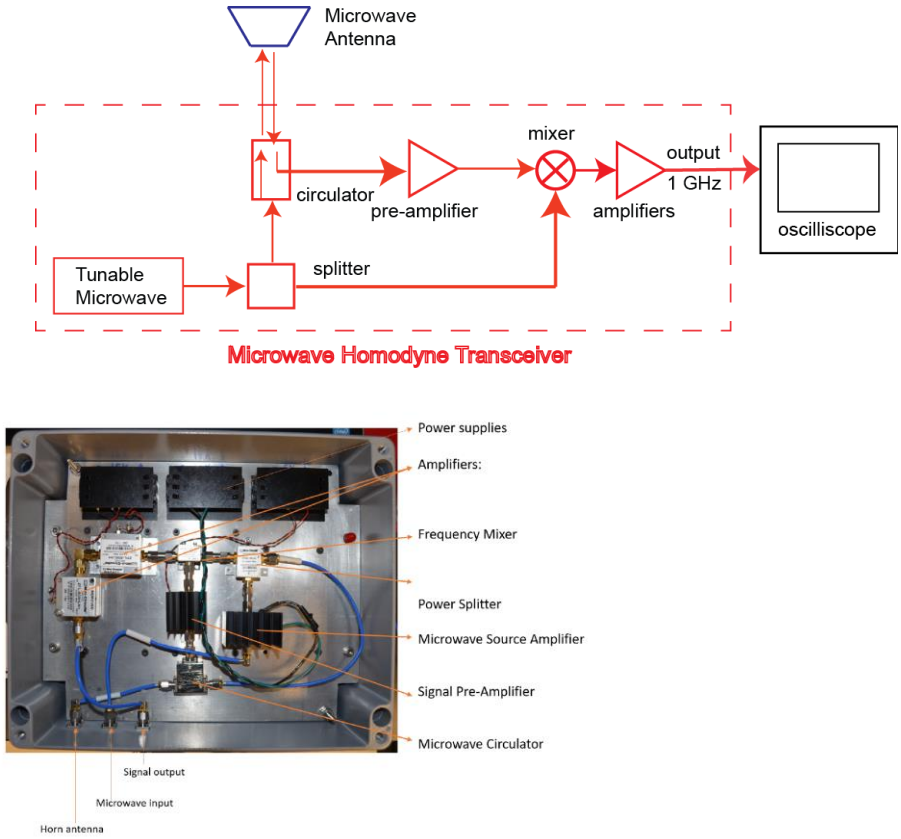


***Figure 2.*** *(a) Schematics of homodyne microwave detection system. The current setup uses a single microwave antenna for transmitting and receiving the microwave signal. A microwave circulator is used to separate the incoming signal from the illuminating one after the pre-amplifier stage. (b) An integrated box for coherent microwave scattering, corresponding to the dashed line box in (a). The whole box is about 10 cm x 10 cm x 5 cm. 'Reproduced from [10].*

Equation (5) shows that the averaged electric field of the microwave scattering is approximately proportional to the field of the incident microwave, the total number of the electrons

inside the plasma, and the frequency of the microwave. So, it is natural to try to use microwave sources at higher frequencies to obtain higher scattering signals from the plasma. Microwave source at 100 GHz has been used in the literature.[11, 12] The drawback is that the skin layer thickness is smaller at higher frequencies, which limits the overall measurement range of electron number densities. The experimental setup at higher frequencies might require two mixers to beat the frequency down to sub gigahertz range for detection.

### 2.3 Quantitative calibration of coherent microwave scattering

Quantitative calibration of coherent microwave is required for quantification of scattering signals. The microwave scattering signal is relative, since it depends on the relative position between microwave horn antenna and the plasma. The microwave reflection and scattering from the equipment in the surrounding environment might generate DC and/or low frequency offsides. The coherent microwave scattering signal can be calibrated by using dielectric materials with well-known dielectric constants (e.g. alumina and PTFE). [13, 14] The detailed calibration strategy and procedure are the following.

The microwave scattering signal from the detection system can be written for the limiting cases of a perfect conductor or a perfect dielectric scatterer placed in the illumination region as follows:

$$\begin{aligned} U_c &= A\sigma V_c \quad , \quad \text{for perfect conductor} \\ U_d &= A\varepsilon_0(\varepsilon_r - 1)\omega_{mw} V_d, \quad \text{for dielectirc material} \end{aligned}$$

where $U_c$ and $U_d$ are the microwave signals for a perfect conductor and dielectric material, respectively, A is the characteristic parameter of the microwave detection system including surrounding environment effects, $\sigma$ is the electrical conductivity of the scatterer, $\varepsilon_r$ is the relative

permittivity of the scatterer, $\varepsilon_0$ is the free space permittivity, $\omega_{mw}$ is the angular frequency of microwave, and $V_c$ and $V_d$ are the volumes of the scatterers, respectively. By measuring the microwave scattering from a sample material with known dielectric properties placed within the illumination region, one may determine the microwave detection system characteristic A at the sample's location. A small cylindrical sample of alumina or PTFE is usually mounted at the laser beam focal point with the cylinder's axis parallel to the laser's propagation direction to provide calibrations for the laser-induced plasmas.

Here an example of calibrating coherent microwave scattering from a laser-induced plasma is shown. The microwave scattering signals from alumina and PTFE are shown in Figure 3. The parameter A was measured to be $80.5\ V \cdot \Omega/cm^2$ and $82.6\ V \cdot \Omega/cm^2$ with alumina and PTFE calibrators, respectively. The measurement of A should be more accurate with the use of alumina due to its larger ε value leading to a stronger scattering signal. With the same detection system and experimental setup, the temporal evolution of total electron number by laser-induced breakdown is shown in Fig. 3(b) with the laser energy inputs of 70, 35 and 16 mJ at 1064, 532 and 355 nm, respectively. By using the system characteristic parameter A and the estimated volume of plasma column, one can determine the conductivity of the plasma column from the microwave signal. The electron density in the plasma can then be determined by using the expression:

$$\sigma = 2.82 \times 10^{-4} n_e \nu_m / (\omega^2 + \nu_m^2)\ \Omega^{-1}\ \text{cm}^{-1}, \quad (6)$$

where $\nu_m$ is the frequency of electron-neutral collisions $\nu_m \approx 2 \times 10^9 p[Torr]\ s^{-1}$ $n_e$ is the electron density ($cm^{-3}$), and ω is the angular frequency ($s^{-1}$). Hence, the total electron number in the plasma can be explicitly expressed

$$N_e = \frac{\varepsilon_0(\varepsilon-1)V_d}{2.82\times10^{-4}} \cdot \frac{U_c}{U_d} \cdot \frac{\omega(\omega^2+\nu_m^2)}{\nu_m} \quad (7)$$

It should be noted that one of the differences between laser-induced plasma and dielectric materials is the time evolution of dielectric constants. The dielectric materials have fixed dielectric constants and fixed volume. The laser-induced plasma has varying dielectric constants and volume. It leads to a fixed DC microwave signal for the dielectric materials, while a temporally varying signal for the plasma, as shown in Figure 3(b). The microwave detection circuit has to be changed to accommodate the relative bandwidth of the signals. As an example, the microwave circuit in Figure 2(a) should remove the amplifiers after the mixer, which usually do not have the bandwidth for DC signals.

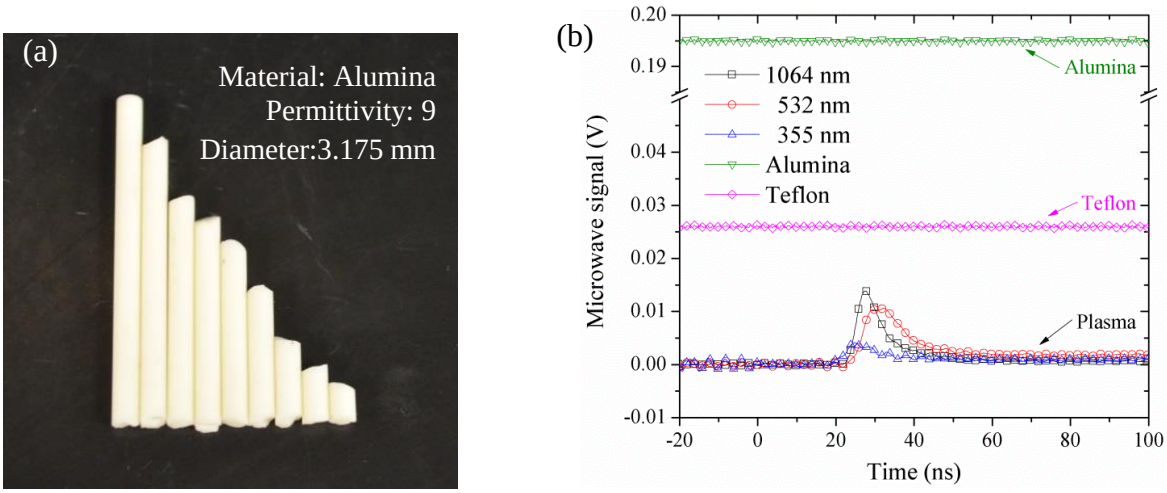


***Figure 3.*** *(a) typical calibration targets made of alumina at 1/8-inch (3.175 mm) diameter. (b)The microwave scattering signals from dielectric materials (alumina and PTFE) and laser-induced air breakdown by using 10 ns 1064, 532, and 355 nm laser beam, respectively. 'Reproduced from [13].*

### 3. Resonance-Enhanced Multiphoton Ionization (REMPI)

Although the first paper about multiphoton absorption appeared as early as the 1930s [9], multiphoton absorption and multiphoton ionization (MPI) were intensively studied only after the invention of the giant pulsed laser because not enough photons were available within a short period time to generate significant multiphoton absorption or ionization for a common light source.[15]

MPI and avalanche ionization are recognized as two important mechanisms in the formation of the laser-induced plasma. MPI provides a few seed electrons and avalanche ionization sequentially multiplies them. Pure multiphoton ionization is greatly enhanced if an intermediate state is single or multiphoton resonant with the laser frequency. By using these resonances, it can become an accurate spectroscopic method for measuring trace species or pollutants [11, 8], which is called Resonance Enhanced MultiPhoton Ionization (REMPI). Common detection methods for the MPI or REMPI signal are based on collection of electrons by electrical probes/electrodes [11, 8] or collection of ions by Time Of Flight (TOF) mass spectroscopy [8]. Both methods require that the electrons or ions be extracted from the ionization region, so neither method directly measures all the free electrons that are generated and neither can follow the electron recombination process with high temporal accuracy.

Radar REMPI is applicable to diagnostics of many atomic and molecular species. Radar REMPI is useful for species which do not fluoresce due to predissociation, or the environmental limitations of limited optical access and/or strong background emissions. Here a summary is given to the previously demonstrated species detections using single ultraviolet and visible laser beam for REMPI. It should be noted that the multiple laser wavelengths can be used to probe various atomic and molecular resonance states [16], which is not included here.

**Table 1.** Demonstrated REMPI schemes for some atomic and molecular species using single laser

| Species | REMPI schemes (single laser wavelength) |
|---|---|
| Atomic hydrogen (H) | 2+1, by 243.1 nm[17-19]<br>3+1, by 364.68 nm[20-22] |
| Atomic Oxygen (O) | 2+1, by 225.6 nm [23-25] |

| | |
|---|---|
| Atomic nitrogen (N) | 2+1, by 225.5-294.5 nm[26, 27] |
| Atomic carbon (C) | 2+1, by 247.5nm[28], 286-287nm, 313.6nm [29] |
| Xenon (Xe) | 2+1, by 223, 224, 225nm [10] |
| Sodium (Na) | 1+1, by 589, 589.6nm [30, 31] |
| Argon (Ar) | 3+1, by 261nm [32]<br>3+1, by 332nm [33] |
| Molecular hydrogen ($H_2$) | 2+1, by 201nm [34, 35]<br>2+1, by 229 – 234 nm for vibrationally excited [36] |
| Molecular oxygen ($O_2$) | 2+1, by 287.5nm [37, 38] |
| Singlet oxygen (O2(a)) | 2+1, by 311–313 nm [39] |
| Molecular Nitrogen ($N_2$) | 3+1, by 283 - 285nm [40] |
| Nitric oxide (NO) | 1+1, by 226nm [12, 41]<br>2+1, by 381nm [42, 43] |
| Carbon Monoxide (CO) | 2+1, by 230nm [41] |
| Formyl radical (HCO) | 2+1, by 373 to 427 nm [44, 45] |
| Methyl Radical ($CH_3$) | 1+1, by 216nm [16]<br>2+1, by 333nm [33, 46] |
| Ethylene ($C_2H_4$) | 2+1, by 338-348nm [47] |

### 3.1 Calculations of REMPI cross sections for atomic species

For atomic species, it is possible to calculate the REMPI cross sections using quantum perturbation and quantum defect theory in two steps. The first step of the REMPI process is multi-photon excitation to an excited state. The second step is multi-photon ionization to the continuum

state to generate plasmas. Including the laser linewidth, natural and pressure broadening effects, the three-photon absorption rate to the intermediate state in ($s^{-1}$) can be calculated as

$$W_{f,g}^{3} = (2\pi\alpha F\omega)^{3}\left|\sum_{|2>}\sum_{|1>}\langle f|r|2\rangle\frac{\langle 2|r|1\rangle}{\sqrt{(\omega_{2,g}-2\omega_{\mathrm{L}})^{2}+\gamma_{2}^{2}/4}}\frac{\langle 1|r|g\rangle}{\sqrt{(\omega_{1,g}-\omega_{\mathrm{L}})^{2}+\gamma_{1}^{2}/4}}\right|^{2} G(\omega_{L})$$

where $g$ and $f$ denote the ground and the intermediate states of the atom, respectively, $\omega_{2,g}$, $\omega_{1,g}$ are the frequency difference between ground state and virtual intermediate states "2" and "1", accordingly (all possible transitions that satisfy the selection rules are taken into account); $\alpha$ is the fine-structure constant (1/137.036). Expressions $\langle * |r| * \rangle$ are the dipole transition matrix elements connecting the ground state, virtual states, and final state $g$, 1, 2, and $f$. $\gamma_i$is the linewidth of the $i$th virtual state. $G$ is a generalized line shape scale factor, which is the convolution of level Lorentz broadening, Doppler broadening, and laser broadening. $G$ is strongly peaked at $\omega_{3,g} = \omega_L$ the threephoton resonance condition.

A quantum-defect approximation is used for the one-photon ionization from the excited bound state of an atom, which is exact for hydrogenic atom and quite good for Rydberg states of rare gases [48]

$$\sigma_{Pi} = \frac{8\times 10^{-22}}{Z(U_I/R)^{1/2}(\hbar\omega_L/U_I)^3}[m^2]$$

where Z is net charge on the ion, $U_I$ is the ionization potential for the atom at the excited state, R is Rydberg constant and $\hbar\omega_L$ is the photon energy.

Here 3+1 REMPI of argon by 261.27nm light is used as an example. In argon the first step of the REMPI process is three-photon excitation to an intermediate level $|f\rangle = 3p^5 3d[5/2]^3$ by

three 261.27 nm photons. The second step is one-photon ionization to the continuum state. A Grotrian diagram for 3+1 REMPI in argon is shown in Figure 4. The dominant channels contributing to the three-photon transition between the ground state $|g\rangle$: $3p^6\ {}^1S_0$and the excited state$|f\rangle$: $p^5\left(\ {}^2P^0_{1/2}\right)3d$: $\ {}^2[5/2]^0_3$ are shown. The principal levels shown on the right hand of the diagram are the ones that are allowed by dipole transition selection rules and contribute significantly to the three-photon transition cross section as the nearest to resonance states.

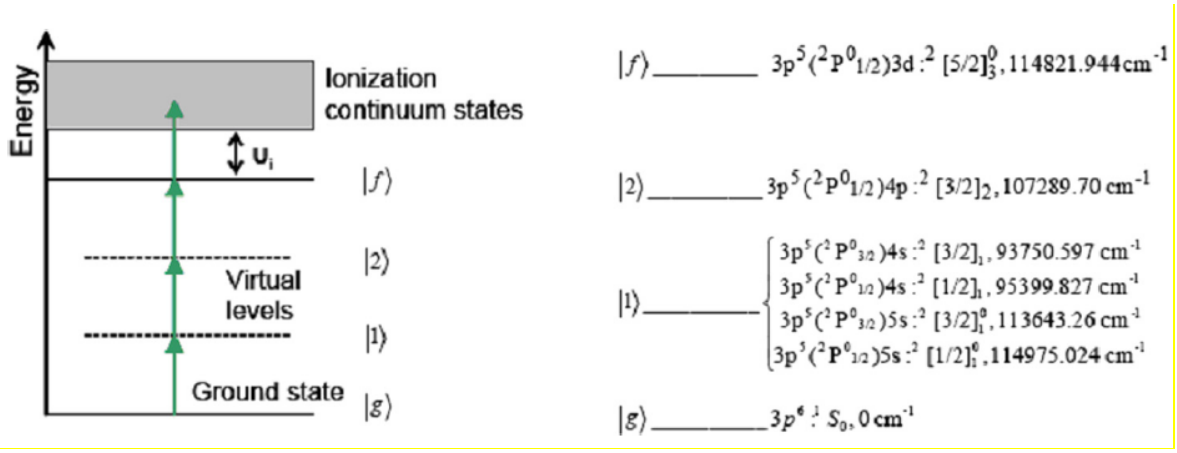


**Figure 4.** Schematic plot of the 3+1 REMPI in argon and the dominant channels that contribute to the three photon transition between the $3p^6\ {}^1S_0$ and the $3p^5\left(\ {}^2P^0_{1/2}\right)3d$: $\ {}^2[5/2]^0_3$ excited state

The three-photon cross-section for metastable state $|f\rangle = 3p^5 3d[5/2]^3$ excitation defined from $W^{(3)}_{fg} = \sigma_{(3)}F^3$ is $\sigma_{(3)} = 2.81 \times 10^{-92}\mathrm{m}^6\mathrm{s}^2$ [48] is the 3-photon probability for excitation of level $|f\rangle$ from the ground state $|g\rangle = 3p^6 1\,S$. $F$ is the total photon flux measured in number of photons per meter-squared per second, $F(r,t) = I_L(r,t)/\hbar\omega_L$, the laser intensity has a Gaussian profile $I_L(r,t) = I_0 \exp\left(-r^2/r_b^2\right)$ for the Ti:Sapphire laser used for argon REMPI process, $r_b$ is the radius of laser focus, $\omega_L$ is the laser angular frequency.

The cross-section for the one-photon ionization from the excited bound state of argon $|f\rangle = 3p^5 3d[5/2]^3$ was calculated on the basis of a quantum defect approximation [32, 49], $\sigma_{Pi} = 7.67 \times 10^{-23}$ m$^2$. The kinetic energy of the free electrons generated by the considering 3+1 REMPI process in argon is $\varepsilon_{ph} = \hbar\omega_L - U_I \approx 3.2$ eV. Here $U_I = I_i - I^*$ is the ionization potential for the atom in the excited state and $\hbar\omega_L$ is the photon energy; $I_i = 15.76$, $I^* = 14.236$ eV are the ionization potential of argon atoms in the ground state and the energy of the excited level $|f\rangle = 3p^5 3d[5/2]^3$.

### 3.2 Calculations of REMPI cross sections for molecular species

Molecular species, including both stable species and radical species can be measured by REMPI. The REMPI cross sections of molecular species are difficult to calculate in general mainly because of the overlapping molecular levels and incomplete intermediate levels. The absolute calibration can be conducted by the atomic species with nearby transitions without using dielectric materials. For example, due to the proximity of argon resonance state *$2s^2 2p^5 4f$ [7/2, J=4]* (4+1 REMPI by 332.5nm) with the state $3p^2 A_2'' 0_0^0$ of $CH_3$ (2+1 REMPI by 333.6nm), argon can be used to calibrate methyl radical concentrations as [33]

$$N(CH_3) = \frac{S(CH_3)}{S(Ar)} \cdot \left( \frac{\sigma^{(4+1)}(Ar)}{\sigma^{(2+1)}(CH_3)} \right) \cdot \frac{I^5}{I^3} \cdot N(Ar)$$

where $N$ is the number density, $S$ is the observed signal, $\sigma$ is the REMPI cross section and $I$ is the laser intensity. The corresponding quantities for $CH_3$ or argon are represented in brackets.

Similar to atomic species, the two-photon absorption cross section of $CH_3$ can be estimated based on time-dependent quantum perturbation theory. The two-photon absorption coefficient is

thus found by multiplying the dipole moments weighted by quantum defects. The two-photon absorption process for $CH_3$ is described as

$$W_{f,g}^{(2)} = (2\pi)(2\pi\alpha)^2 F(r,t)^2 \omega_L^2 \left| \sum_1 \frac{\langle f|r|1\rangle\langle 1|r|g\rangle}{\sqrt{(\omega_{1g}-\omega_L)^2+\gamma^2/4}} \right|^2 \cdot FC \cdot G(\omega_L) \qquad (8)$$

where *FC* is the Franck-Condon factor for the excited state, which was taken as 0.91.[50]

Instead of using Einstein coefficients to calculate the dipole moments as is done for atomic species, the absorption coefficients or oscillator strengths can be used to calculate the first-order dipole moments of various transitions for $CH_3$. The dipole moments of $CH_3$ is calculated from the oscillator strengths and absorption coefficients from[51]

$$f(a \to b) = \frac{2}{3}\frac{m_e}{\hbar e^2}(E_b - E_a)Q(a \to b)|R_{ab}|^2 \qquad (9)$$

where $m_e$ and $e$ are the electronic mass and charge, respectively, $\hbar$ is Planck constant $h/2\pi$, $Q(a \to b)$ is the angular factors resulting from the angular integration [51], and the radial transition moment integral is defined as

$$R_{ab} = \left\langle R_a(r)\middle|r\middle|R_b(r)\right\rangle \quad . \qquad (10)$$

For $CH_3$, the absorption coefficient and oscillator strength were found in references [52, 53]. The transitions from the virtual state to the excited state were from reference [51]. The predissociation fraction of the excited state $3p^2A_2''0_0^0$ was set as 54% [54]. The parameters used in the calculations are summarized in *Table 2*. The two-photon absorption cross section for $CH_3$ was found to be $3.1\times10^{-47}$ $cm^4 \cdot sec^2$ for the laser linewidth of 0.01 nm at 333.6nm.

*Table 2. Parameters used in the calculation of the cross section of $CH_3$*

| Transition between the ground state and intermediate states (IS) | |
|---|---|
| IS: 3s $^2A_1'$ | $3s^2A_1'$-X, wavelength = 216.4nm, Q = 4/15, f=0.012 |
| IS: 3d $^2E$ | $3d^2E''$-X, wavelength = 149.7nm, Q =4/15, f=0.014 |
| IS: 3d $^2A_1'$ | $3d^2A_1'$-X, wavelength = 150.3nm, Q = 0.4, f=0.004 |
| Transition between the intermediate states (IS) and the excited state of $3p^2A_2''0_0^0$ | |
| IS: 3s $^2A_1'$ | $3p^2\ A^2$ - $3s^2A_1'$, wavelength = 728nm, Q = 1/3, f=$2\times10^{-5}$ |
| IS: 3d $^2E$ | $3p^2\ A^2$ - $3d^2E''$, wavelength = 1520nm, Q =0.4, f=0.03 |
| IS: 3d $^2A_1'$ | $3p^2\ A^2$ - $3d^2A_1'$, wavelength = 1461nm, Q = 4/15, f=0.021 |

## 4. Plasma Characterization by Coherent Microwave Scattering

### 4.1 REMPI and Avalanche Plasma Modeling

Coherent microwave Rayleigh scattering can accurately follow the temporal evolution of total free electrons in the selectively formed REMPI plasma: both generation and decay, which can be used plasma model development, calibration, and validations. Since the REMPI plasma can be approximated as an elongated ellipsoid with its length >> its radius (characteristic length ~ 1 mm, radius 20-50 μm), one-dimensional modeling of plasma in a cylindrical geometry with an axis directed along the laser beam is justified. Thus, if the microwave radiation is linearly polarized with the electric field vector coinciding with the direction of the major axis of the plasma, the electric field of the scattered microwave signal is linearly proportional to $2\pi \int_0^\infty r n_e(r,t)dr$, i.e., total electron number inside the REMPI plasma.

A partially ionized REMPI plasma in a single component inert gas argon is considered here. Even in this a simple case, the composition of the plasma is rather complicated with detailed plasma chemistry. In the theoretical model, it is necessary to take into account at least the neutral component in the ground state, the excited atoms involving in the REMPI process, electrons number density ($n_e$), atomic ion number density $Ar^+$ ($n_{+,1}$), as well as the formation of molecular

ions $Ar_2^+$ $(n_{+,2})$ at elevated pressures in three-body processes: $Ar^+ + Ar + Ar \rightarrow Ar_2^+ + Ar$. With the formation of molecular ions, the recombination decay of the plasma is accelerated because three-body recombination processes involving atomic ions $Ar^+$ are supplemented by rapid dissociative recombination of molecular ions $Ar_2^+$. As shown in experiments, this is reflected in the detected signal of microwave scattering on the decaying REMPI plasma.[55]

Plasma dynamics in the diffusion-drift approximation can be formulated as in [32, 55, 56]. The continuity equation for the density of excited atoms in $|f\rangle = 3p^5 3d[5/2]^3$

$$\frac{\partial N^*}{\partial t} + \frac{1}{r}\frac{\partial}{\partial r}(r\Gamma^*) = N_g \sigma_{(3)} F^3 - N^*(\sigma_{Pi} F + \text{Radiative and Quenching Losses}) \qquad (11)$$

with the initial condition $N^*(t=0) = 0$, and boundary conditions $\left.\frac{\partial N^*}{\partial r}\right|_{r=0} = 0$ and $N^*(\infty) = 0$, where $N_g$ is the number density of argon atoms in the ground state $|g\rangle = 3p^6 1\,S$, $\Gamma^*(r,t) = N^* u - D^* \frac{\partial N^*}{\partial r}$ is the radial flux of the excited argon atoms; $u(r,t)$ is the background gas flow rate; $D^*$ is the diffusion coefficient of the excited atoms. 1-photon ionization $N^* \sigma_{Pi} F$ and all the main loss mechanisms: radiation and in pair and triple collisions with neutral atoms and deactivation in collisions with electrons are taken into account in (11).

For the diffusion coefficients of metastable argon atoms in argon [32, 56], $D^* = 7.3 \times 10^{-6} (T_{[K]}/273)^{1.5}\,(760/p_{[Torr]})$ $m^2 s^{-1}$. [57] This value is approximately half of the diffusion coefficient of unexcited argon atoms in their own gas (self-diffusion coefficient). For a mixture of gases, for example argon and xenon [56], the diffusion coefficient of the excited argon atoms, $D^* = D_{12}$, where $D_{12}$ is the diffusion coefficient of the gas component in the binary gas mixture estimated as $D_{12} \approx \sqrt{\frac{3kT}{M_1 M_2}\left(z_1 x_2 M_2^{1/2} + z_2 x_1 M_1^{1/2}\right)}$, $z_i = \frac{1}{n_i \sigma_{ii} + n_j \sigma_{ij}\left[1+(M_i/M_j)^{1/2}\right]}$ $(i,j) =$

1,2), $\sigma_{12} = \sigma_{21} \approx \frac{\pi}{4}(d_1 + d_2)^2$.[58] Here $M_1, M_2$ are atom masses, $x_1, x_2$ are the partial pressure fractions, and $d_1, d_2$ are effective diameters of the argon and xenon atoms correspondingly.

The continuity equations for all charged components of the plasma, electrons, and ions are

$$\frac{\partial n_{e,+1,+2}}{\partial t} + \frac{1}{r}\frac{\partial}{\partial r}\left(r\Gamma_{e.+1,+2}\right) = (Generation - Losses)_{e,+1.+2}, \qquad (12)$$

where

$$\Gamma_{\mathrm{e}}(r,t) = n_e u - \mu_e n_e E - D_e \frac{\partial n_e}{\partial r} - D_e \frac{n_e}{T_e}\frac{\partial T_e}{\partial r} = n_e u_e \qquad \text{and}$$

$$\Gamma_{+1,+2}(r,t) = n_{+1,+2} u + \mu_{+1,+2} n_{+1.+2} E - D_{+1,+2}\frac{\partial n_{+1,+2}}{\partial r} = n_{+1,+2} u_{+,2+}$$

are fluxes of electrons and ions in the diffusion-drift approximation in the laboratory frame of reference associated with the axis of symmetry of the plasma. In the expressions for the flows, it is taken into account that the gas can be set in motion, and $u_e, u_+, u_{2+}$ and $u$ are charged particles and bulk gas velocities in a laboratory reference frame (related to a plasma channel axis). In the equation for the electron flux $\Gamma_{\mathrm{e}}$, the thermal diffusion flux associated with the electron temperature gradient is included. $\mu_{e,+1,+2}, D_{e,+1,+2}$ are mobilities and diffusion coefficients for electrons and atomic and molecular ions, respectively. For the flow of the atoms at the excited states, charge transfer with background gas is taken into account in expressions for electron and ion flows.

The initial and boundary conditions for the equations of continuity (10)

$n_{e,+1,+2}(t = 0) = 0$, and $\left.\frac{\partial n_{e,+1,+2}}{\partial r}\right|_{r=0} = 0$ and $n_{e,+1,+2}(\infty) = 0$, respectively.

The right-hand side of the continuity equations (10) includes all the mechanisms of electron and ion generation by REMPI, avalanche ionization, the conversion of atomic ions to molecular ions, and the loss of charges in all the main recombination processes. Details and all relevant reactions and rates can be found in the references.[32, 55, 56, 59]

The expansion of the plasma leads to the appearance of a radial field and the transition to the regime of ambipolar diffusion. Therefore, the system of equations for plasma implantation must be solved together with the equation for the distribution of potential (Poisson equation)

$$\frac{1}{r}\frac{\partial}{\partial r}\left(r\frac{\partial \varphi}{\partial r}\right) = -\frac{e}{\varepsilon_0}(n_{+1} + n_{+2} - n_e), \qquad (13)$$

with the boundary conditions $\left.\frac{\partial \varphi}{\partial r}\right|_{r=0} = 0$ and $\varphi(\infty) = 0$. Corresponding electric field is

$$E(r,t) = -\frac{\partial \varphi}{\partial r}. \qquad (14)$$

The temperature of all ions is assumed equal to the local gas temperature, $T_{+1} = T_{+2} = T(r,T)$ and less than $T_e(r,t)$. The electron temperature in the plasma obeys a hydrodynamic equation [55]

$$\frac{\partial}{\partial t}\left(\frac{3}{2}n_e k T_e\right) + \frac{1}{r}\frac{\partial}{\partial r}\left[r\left(\frac{5}{2}\Gamma_e k T_e - \lambda_e \frac{\partial T_e}{\partial r}\right)\right] = J_L + J_{MW}$$
$$-\frac{3}{2}n_e k(T_e - T)\left(\nu_m + \nu_{e,+} + \tfrac{1}{2}\nu_{e,2+}\right)\delta + N^* \sigma_{Pi} F \varepsilon_{ph} + k_e N^* n_e I^* - \nu_{i,av} n_e I_i, \qquad (15)$$

where $J_L = e^2 n_e I_L(r,t)(\nu_m + \nu_{e,+} + \nu_{e,2+})/\varepsilon_0 mc\left[\omega_L^2 + (\nu_m + \nu_{e,+} + \nu_{e,2+})^2\right]$ and $J_{MW} = e^2 n_e I_{MW}(r,t)(\nu_m + \nu_{e,+} + \nu_{e,2+})/\varepsilon_0 mc\left[\omega_{MW}^2 + (\nu_m + \nu_{e,+} + \nu_{e,2+})^2\right] << J_L$ are, respectively, the Joule heating by the laser pulse and the microwave (note: to make microwave scattering diagnostics completely nonintrusive, microwave intensity, $I_{MW}$, has to be small enough not to induce additional heating of electrons, as in all REMPI experiments); $\delta = 2m/M$ is the collision constant of electrons with neutrals or ions. New electrons appear in the process of REMPI with energy $\varepsilon_{ph}$, heat transfer is carried out by convective transfer with an electron flux and electronic heat conduction mechanism with coefficient $\lambda_e = \frac{5}{2}k n_e D_e$, and the electrons are heated by quenching excited atoms, with the quenching constant $k_e$, as well as the electron energy loss rate due to the avalanche ionization by electrons oscillating in the laser field, $\nu_{i,av} n_e I_i$. The initial and

boundary conditions for the electronic heat conduction equation (13), which is solved together with the equations (9) - (12), are

$T_e(t=0) = T(t=0) = T_0 = 300\ K$, and $\left.\frac{\partial T_e}{\partial r}\right|_{r=0} = 0$ and $T_e(\infty) = T_0$.

To calculate the perturbation of the background gas, the equations of gas dynamics and the equation of state of the gas must be taken into account. The gas becomes involved in the motion not only by the pressure gradient due to the heating, but also by the momentum transfer from the charged particles to gas atoms. The gas flow arising as a result of cooling and ambipolar expansion of REMPI generated plasma can be described in terms of one-dimensional axisymmetric equations of a compressible viscous gas [54].

$$\frac{\partial \rho}{\partial t} + \frac{1}{r}\frac{\partial (r\rho u)}{\partial r} = q_\rho, \tag{16}$$

$$\frac{\partial \rho u}{\partial t} + \frac{1}{r}\frac{\partial (r\rho u^2)}{\partial r} = -\frac{\partial p}{\partial r} + \frac{1}{r}\frac{\partial}{\partial r}(r\tau_{rr}) + F_d, \tag{17}$$

$$\frac{\partial \rho(\varepsilon+\frac{u^2}{2})}{\partial t} + \frac{1}{r}\frac{\partial \{r\left[\rho\left(\varepsilon+\frac{u^2}{2}\right)+p\right]u\}}{\partial r} = Q + \frac{1}{r}\frac{\partial}{\partial r}\left(r\lambda\frac{\partial T}{\partial r}\right) + \frac{2}{3}\frac{\eta}{r}\frac{\partial}{\partial r}\left(ru\left(2\frac{\partial u}{\partial r} - \frac{u}{r}\right)\right) + Q_d, \tag{18}$$

$$p \approx \frac{k\rho T}{M} = (\gamma - 1)\rho\varepsilon. \tag{19}$$

Here, $\rho = MN_g$ is the density of the bulk gas, $M, N_g$ are the mass of an atom and the density of atoms of a non-ionized gas, respectively; $\varepsilon$ is internal energy per unit mass of the neutral component, $\gamma$ is the specific heat ratio (for the monatomic ideal gas considered as an example $\gamma = 1.667$); $\lambda$ and $\eta$ are gas heat conductivity and viscosity; $Q$ is the heat source

$$Q(r,t) = \frac{3}{2}n_e k(T_e - T)\left(\nu_{en} + \nu_{e,+} + \frac{1}{2}\nu_{e,2+}\right)\delta + \beta_d n_e n_{+2}(I_i - \varepsilon_d), \tag{20}$$

where the first term is due to the relaxation of electrons in collisions with atoms and ions and the second is gas heating in a process of dissociative recombination of electrons and molecular ions; $\varepsilon_d$ ≈1 eV is the affinity energy of the $Ar_2^+$ ion. In the heat source (5*), we did not take into account the heat release as a result of the recombination of atomic ions, as this excess energy is carried away by radiation (photorecombination) or is given to an electron participating in the three-body recombination process. [60] In the gas dynamics equations Eqs. (16) -(20) we

included the rate of loss and generation of neutral atoms in processes of ionization and recombination.

$$q_\rho = M(-\nu_i n_e - N^* \sigma_{Pi} F - k_{conv} n_{+1} N_g^2 + \beta_{eff} n_e n_{+2} + 2\beta_d n_e n_{+2}), \quad (21)$$

the friction forces between the charged particles and atoms

$$F_d = m\nu_{en} n_e (u_e - u) + \tfrac{1}{2} M \nu_{+,n} n_{+1} (u_+ - u) + \tfrac{2}{3} M \nu_{2+,n} n_{+2} (u_{2+} - u), \quad (22)$$

and an additional heat source resulting from the action of friction forces:

$$Q_d = m\nu_{en} n_e (u_e - u)^2 + \tfrac{1}{2} M \nu_{+,n} n_{+1} (u_+ - u)^2 + \tfrac{2}{3} M \nu_{2+,n} n_{+2} (u_{2+} - u)^2. \quad (22)$$

As a result of this interaction, an acoustic disturbance arises which was recently detected experimentally [37]. At a low degree of ionization, $n_e/N_g < 10^{-5}$, the gas-dynamic effects associated with the heating of the gas and its hydrodynamic flow are negligible.

Examples of calculation of REMPI plasma and gas dynamics parameters evolution and comparison with experiment for argon are shown in Figure 5-7.

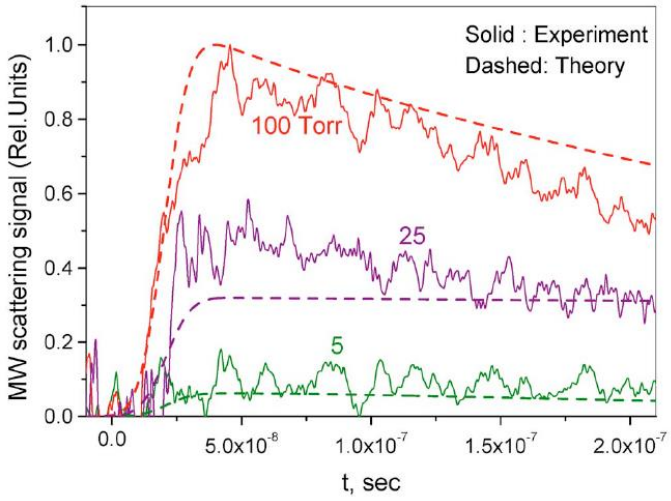


Figure 5. Comparison between experimental and theoretical results of microwave scattering from plasma produced by REMPI in argon at different pressures. Laser wavelength is 261.27 nm, linewidth=0.1 nm, laser focal radius is $r_b$=7.5 μm; energy per pulse E=2.1 mJ. All results presented here correspond to the same laser beam parameters. 'Reproduced from [55].

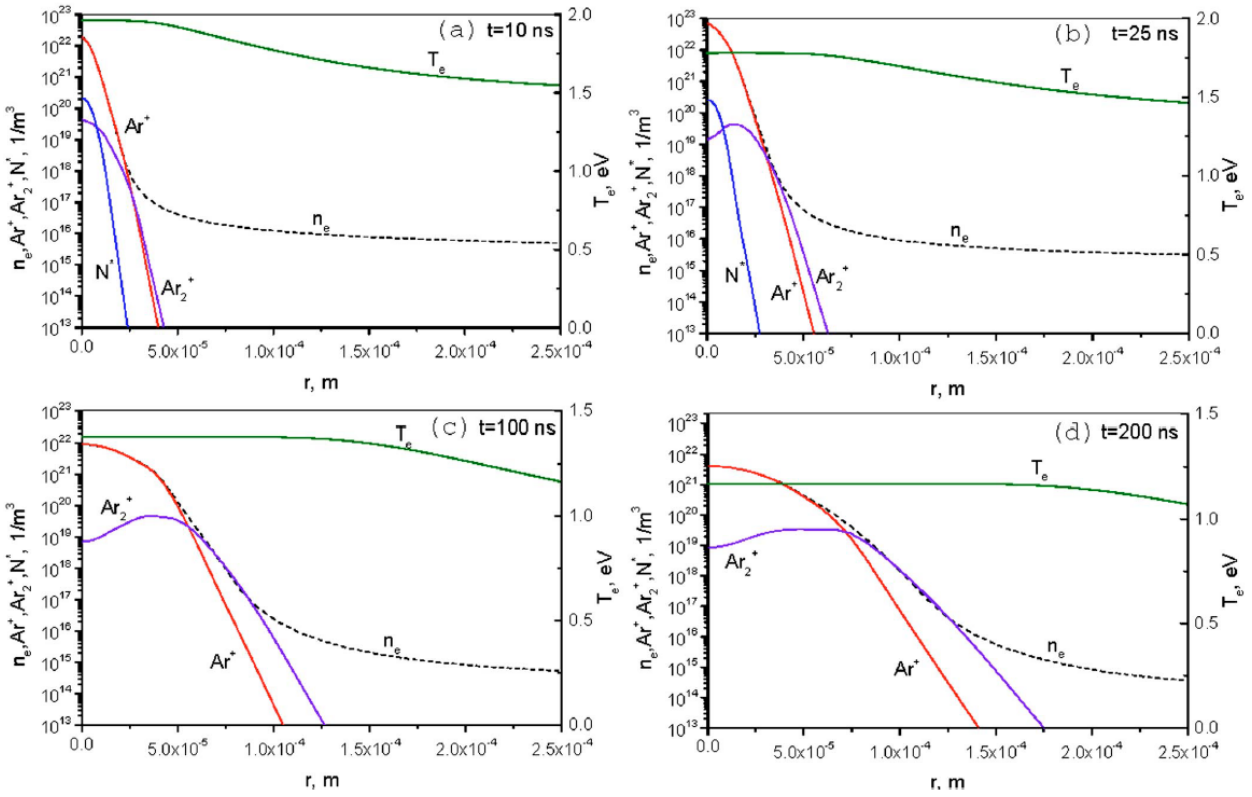


Figure 6. The plasma evolution at different times: (a) t=10 ns; (b) 25 ns; (c) 100 ns; and (d) 200 ns: p=100 Torr; E=2.1 mJ/ pulse. 'Reproduced from [55]

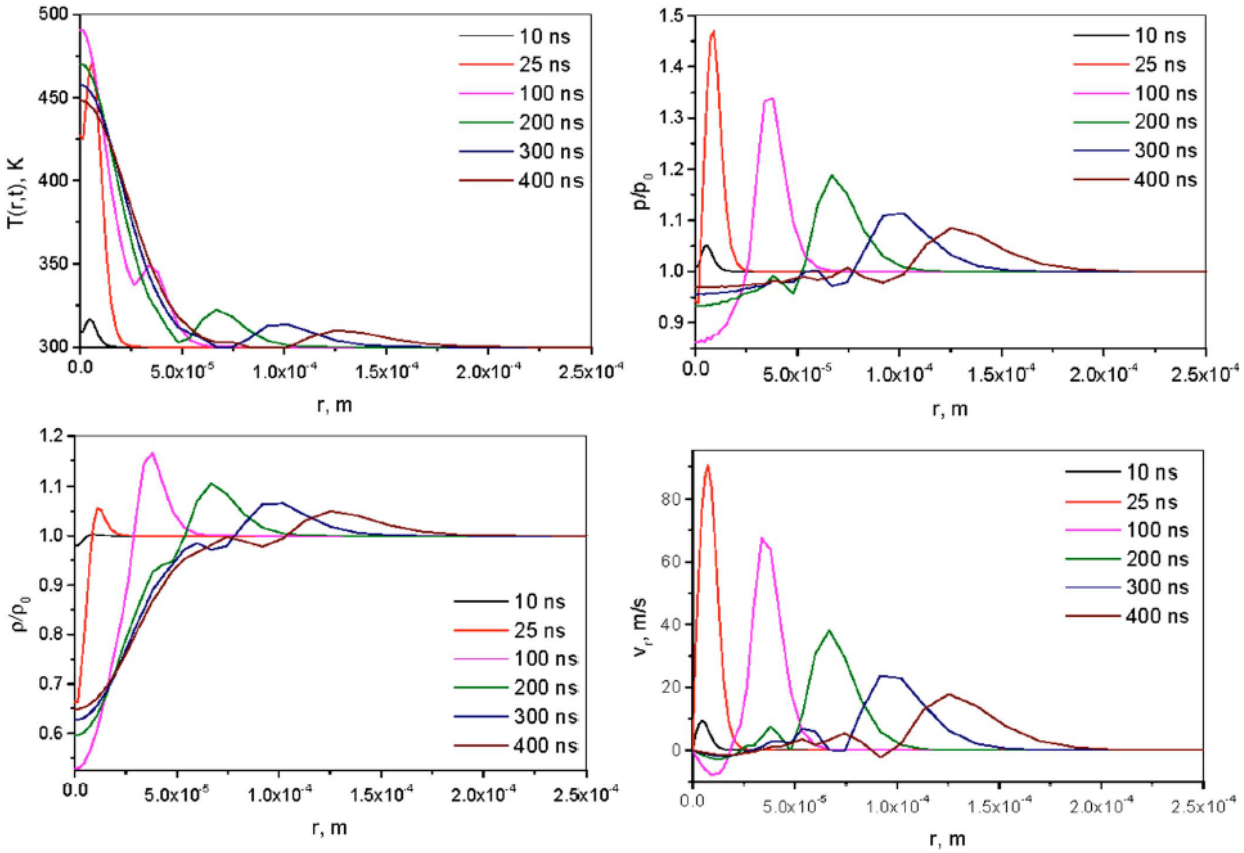


Figure 7. Radial distributions of the gas parameters at different time moments: p=100 Torr; E=2.1 mJ/ pulse. 'Reproduced from [55].

REMPI plasma expansion (Figure 6) represents a classical ambipolar diffusion. It is shown that gas becomes involved in the motion not only by the pressure gradient due to the heating, but also because of momentum transfer from the charged particles to gas atoms. Gas heating and momentum transfer from the charged particles result in a weak shock or acoustic wave. This acoustic signal is maximal when the laser is tuned to REMPI and can be used in diagnostics based on the detection of an acoustic signal instead of scattered microwave. [37] The time dependence of the total number of electrons computed in theory is in agreement with the results of the coherent microwave scattering experiment. The electrons generated by REMPI has an elevated temperature, which dissipate the energy to heat up the surrounding gas after the laser pulse has passed.

The present theory can be easily generalized for REMPI plasma in a multicomponent gas mixture with combined mechanisms of laser breakdown: REMPI ionization of one of the mixture components with subsequent avalanche ionization of another component. [55, 56] This may find many applications because of a drastic reduction of the laser breakdown threshold. It should be noted that the hydrodynamic diffusion-drift approximation reflects well the plasma dynamics in the pressure range exceeding several Torr, when the electron mean free path < characteristic plasma radius. For example, a direct comparison of the diffusion-drift solution with kinetic PIC calculations showed good agreement between the calculations at a pressure of 5 Torr.[59] At lower pressures, kinetic calculation methods are more appropriate.

**On the necessary conditions for avalanche ionization for plasma amplification**

The two-step laser-induced gas ionization (REMPI and subsequent avalanche ionization) may be used to increase the detection sensitivity for trace species at very low concentrations. An initial low density of electrons is produced through ionization of the trace species in air or other gases by REMPI, further subcritical avalanche ionization of the host gas increases the overall density of electrons and improves detectability. It has been shown in the mixture of argon/xenon[56] N2/O2[61] and xenon in air[10].

For this two-step process to be effective in gases and gas mixtures, a certain minimal electron number density must be created by the pre-ionizing REMPI or fs laser pulses. The minimal requirements for the first pre-ionizing pulse to initiate avalanche ionization and significant gas heating by the subsequent pulse should be satisfied. [59] Similar conditions are also valid for a relatively long ionizing laser pulse focused in a gas mixture with REMPI of one mixture component with the subsequent avalanche development in the buffer gas. If the gas is pre-ionized, the avalanche ionization in the subsequent laser pulse occurs at much lower laser intensities than

the breakdown threshold if the ambipolar diffusion replaces free diffusion. This occurs when the plasma density is so high that the radius of the pre-ionized region is larger than the radius of laser focal area, $r_b \gg \lambda_D$. Therefore, the plasma density generated by REMPI is so high that the diffusion becomes ambipolar and the radial ambipolar field suppresses the electron radial losses, which can be estimated as $n_e \approx n_+ \gg \varepsilon_0 k T_e/(e^2 r_b^2)$. For example, assuming that $T_e \approx 1$ eV, $r_b = 100$ μm the development of avalanche ionization is possible at the REMPI preionization $n_e \gg 5.5 \times 10^9$ cm$^{-3}$.

### 4.2 Experimental Plasma Measurements and Characterization

*(a) Electron number density measurement in the laser-induced plasma and breakdown*

Since the invention of the giant pulse laser in the 1960s, laser-induced plasma and breakdown processes have been extensively studied due to its wide applications in scientific and engineering fields with minimal system complexity. Laser-induced breakdown starts with the generation of seed electrons via multiphoton ionization (MPI) process, in which a gaseous atom or molecule simultaneously absorbs multiple photons to be ionized. The seed electrons are then accelerated by the beam's electromagnetic field via the inverse Bremsstrahlung effect. If a sufficient field is applied, the electrons are accelerated to energies that cause electron impact ionization upon collisions with the neutral gas atoms and molecules. The newly liberated electrons then are accelerated by the field leading to an electron avalanche ionization (EAI) process during the laser pulse duration. The EAI process manifests as a visible laser spark which emits light and heats the surrounding medium producing a shock wave that propagates from the breakdown region. Laser-induced gas breakdown was commonly detected by human eyes, photodiodes, and/or cameras with a probability-based criterion. Typically, this criterion is the visible observation of a glow or flash in the focal region for a probability of 10%-50% of the laser firings.

Coherent microwave scattering has been used for temporally resolved measurements of total electron number during the laser-induced plasma and breakdown processes from room pressure up to 40 bar. [62-64] With the measured microwave signals and estimated plasma column, the total electron number during the laser-induced breakdown process for the 10 ns beam at 1064 nm, 532 nm, and 355 nm wavelengths is calculated as shown in figures 8(a), (b), and (c) respectively. In these three figures the laser-induced breakdown in air was measured for pressures ranging from atmospheric to 40 $bar_g$. The total electron number is presented as a function of the laser intensity. For the first two conditions (Fig. 8(a) and (b)) and their corresponding laser wavelengths, there is a threshold intensity. Below the threshold intensity, at a given pressure condition, the total electron number profile is relatively independent of laser intensity. Above the threshold value, the total electron number increases significantly with increasing laser intensity. The threshold intensity is mostly seen for the longer laser wavelengths and lower pressure conditions. It should be noted that the skin layer thickness at higher electron number density might decrease the microwave scattering intensity from the laser-induced spark.

These threshold intensities for inducing laser-induced breakdown with a 1064 nm beam are roughly an order of magnitude higher than threshold intensities for the 532 nm and 355 nm beams. Additionally, for laser intensities below the breakdown threshold, the 1064 nm and 532 nm beams have detectable total electron numbers on the order of ~$10^5$. The 355 nm beam at similar intensities has about an order of magnitude higher total electron number (~$10^6$). This is mostly likely due to higher energy photons of the UV beam producing more electrons during the MPI process, i.e., at 355nm, the MPI dominates while at 1064nm a more stochastic AI dominates the plasma generation

For all three wavelengths, it is clearly shown that increasing the pressure leads to more efficient electron production for a given laser intensity. A small amount of electrons ($10^5$) was measured

at the 0 $bar_g$ pressure condition. When the pressure is above 10 $bar_g$ the total electron number increases to above $10^6$. At pressures above 10 $bar_g$, the total electron number dramatically increases with small increases in laser intensity. This indicates that the EAI process is dominant for elevated pressures for laser-induced breakdown.

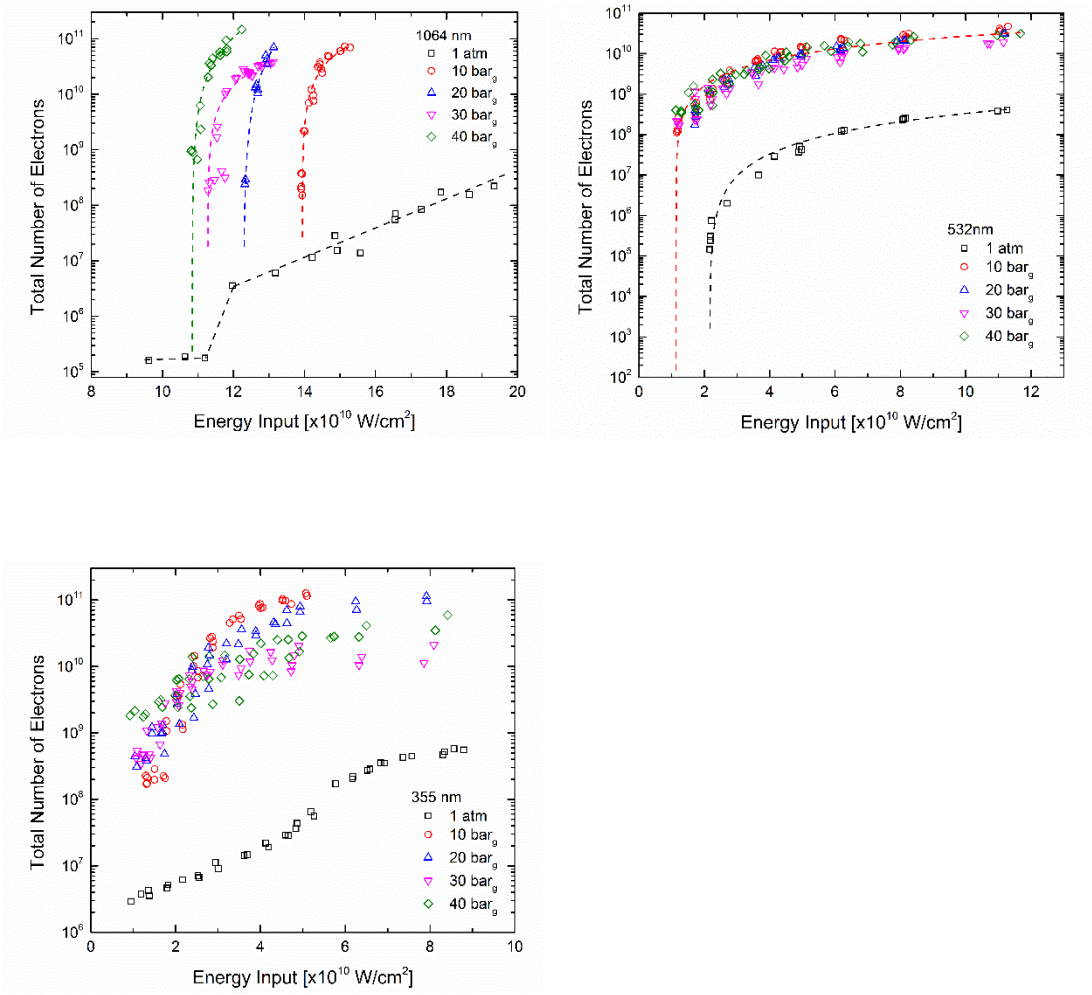


***Figure 8.*** *(a) Total number of electrons versus laser intensity for the 1064 nm wavelength beam, showing strong dependence of breakdown threshold on laser pulse energy at elevated pressures. (b). Total number of electrons versus laser intensity for the 532 nm wavelength beam. Compared to laser-induced breakdown by 1064nm beam, similar trend for weaker dependence of breakdown threshold on laser pulse energy at elevated pressures was observed. (c). Total number of electrons*

*versus laser intensity for the 355 nm wavelength beam. Compared to the laser induced breakdown by 1064nm and 532nm beams, the weakest dependence of breakdown threshold on laser pulse energy at elevated pressures was observed. 'Reproduced from [13].*

*(b) Measurements of Attachment and Cluster Ion Recombination Rates*

Plasma kinetics plays essential roles in atmospheric chemistry, plasma modeling, material processing, and biomedical applications. Unfortunately, many key plasma kinetic reaction rates are not accurately measured. Some existing techniques have limitations to low density gases, and not applicable to atmospheric pressure, which leads to extrapolation of some measurements conducted at low pressure to higher pressures. [12]

In general, REMPI can be used to generate a small volume plasma with known electron number density in a targeted buffer gas at arbitrary temperature and pressures, i.e., a well-controlled plasma reactor. Coherent microwave scattering can directly measure the local electron number density within the REMPI plasma. Radar REMPI has been demonstrated for measurements of attachment [12], three-body recombination[30], and cluster ion recombination[31] at different conditions.

The attachment rate has been determined by swarm techniques and by microwave studies of electron loss rates. These methods, however, are limited to low density gases, and as such, are not applicable at atmospheric pressure in air. As a result, attachment rates at atmospheric and higher densities have been estimated by extrapolation of data measured at low densities. As with the microwave techniques, recent measurements at atmospheric pressure using standard techniques based on filament conductivity dynamics are probing large volumes and are not suitable for local measurements.

In [12], a small volume ($10^{-5}$ $cm^3$) weakly ionized ($10^{-6}$) plasma is created with a 100 ps laser via REMPI of trace amounts of nitric oxide (NO) seeded into atmospheric pressure air. The electron loss rate is subsequently measured by monitoring the plasma density dynamics on a sub-nanosecond time scale using microwave scattering. By fitting the data with simple analytical curves, the electron attachment rate to oxygen in atmospheric pressure air and the dissociative recombination rate in nitrogen has been directly measured. The measured oxygen attachment rate in dry atmospheric pressure air of $0.76 \times 10^8 s^{-1}$. Figure 10 shows the microwave scattering signal and electron attachment to oxygen (circles) and recombination (squares) rates measured for different trace amounts of NO.

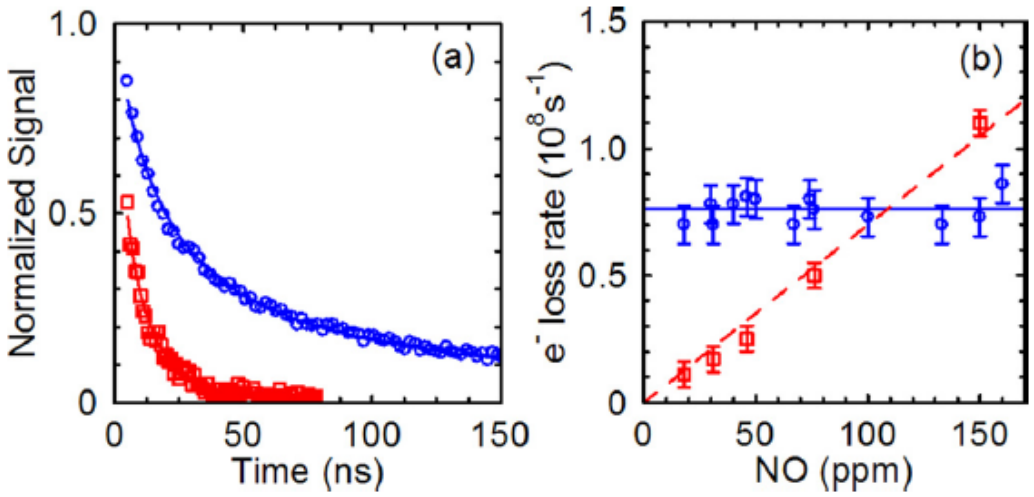


*Figure 9. (a) Microwave scattering dynamics from weak plasma induced in 76 ppm of NO in 1 atm of nitrogen (circles) and air (squares). The solid lines represent least square fits for electron loss. (b) Electron attachment to oxygen (circles) and recombination (squares) rates measured for different trace amounts of NO. 'Reproduced from [12].*

Cluster ion recombination has been measured by Radar REMPI.[31] A laser beam resonantly ionizes sodium atoms by 2+1 REMPI process in the mixture of sodium and argon at pressure from 1 to 760 Torr and temperatures of 300K to ~800K. The sodium cation clusters to argon forming $Na^+(Ar)$ which undergoes dissociative recombination. In this approach, a high concentration $Na^+$ plasma was generated while minimizing generation of all other cation species. In-situ measurement of the alkali plasma recombination processes was made without extracting the electrons or cations by coherent microwave scattering.

*Figure 11* shows the comparison between experimental measurement of the sodium argon plasma decay by coherent microwave scattering and a zero dimensional model. Coherent microwave scattering directly measures the evolution of total electron number in the REMPI plasma. A zero dimensional model was built to extract the temporal evolution of the sodium argon plasma. In the zero dimensional model, sodium argon cluster ions ($Na^+ \cdot (Ar)$ ) were formed in a three body process,

$$Na^+ + Ar + Ar \leftrightarrow Na^+ \cdot (Ar) + Ar \qquad (23)$$

$Na^+ \cdot (Ar)$ dissociative recombination $Na^+ \cdot (Ar) + e \rightarrow Na + Ar$ was determined to be $\beta_{Na^+Ar} = 1.8^{+0.7}_{-0.5}\ 10^{-6} cm^3/s$ for argon at 100 Torr and sodium number density at $5.5\times10^{10}/cm^3$ at 473K.

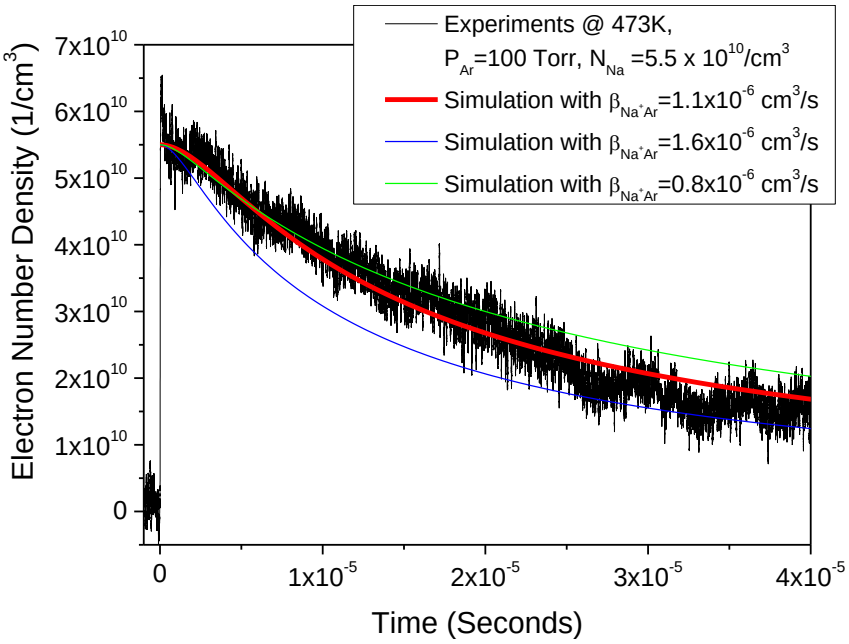


***Figure 10.*** *Comparison of normalized experimental microwave signal from plasma produced by REMPI and avalanche ionization in Na:Ar mixture at sodium number density of $5.5\times10^{10}/cm^3$. 'Reproduced from [31].*

*(c) Measurements of Multiphoton Ionization (MPI) Cross Sections*

As discussed previously, MPI plays key roles in all laser-induced plasma and mass spectroscopy. Basic physical constants of the MPI process, namely photoionization rates and cross-sections, have not been precisely determined in direct experiments. [65]

The cross-section of the MPI is determined experimentally based on absolute measurement of total electron numbers ($N_e$) generated by a femtosecond laser pulse and precise measurements of the laser pulse characteristics.[65] Figure 11(a) presents a typical temporal evolution of the number of electrons and amplitude of scattered microwave signal for two values of intensity: $I_0$ = $2.68 \times 10^{13}$ W/cm$^2$ and $2.93 \times 10^{13}$W/cm$^2$. Right and left vertical axes indicate the signal directly

measured by the RMS and the total number of electrons in the plasma volume Ne determined using the approach described in Methods. It was observed that plasma decayed faster for larger laser intensities; specifically, two-fold decay occurs on characteristic times 2.5 ns and 2 ns for laser intensity of I = 2.68 × $10^{13}$ W/cm$^2$ and 2.93 × $10^{13}$W/cm$^2$, respectively. MPI cross-section σ8 by fitting the measured dependence of $N_e$ versus $I_0$ is shown in Fig. 11(b). Direct measurement of absolute plasma electron numbers generated at MPI of air, and subsequently determine the ionization rate and cross-section of eight-photon ionization of oxygen molecule by 800 nm photons $\sigma_8 = (3.3 \pm 0.3) \times 10^{-130}\ W^{-8}\, m^{16}\, s^{-1}$.

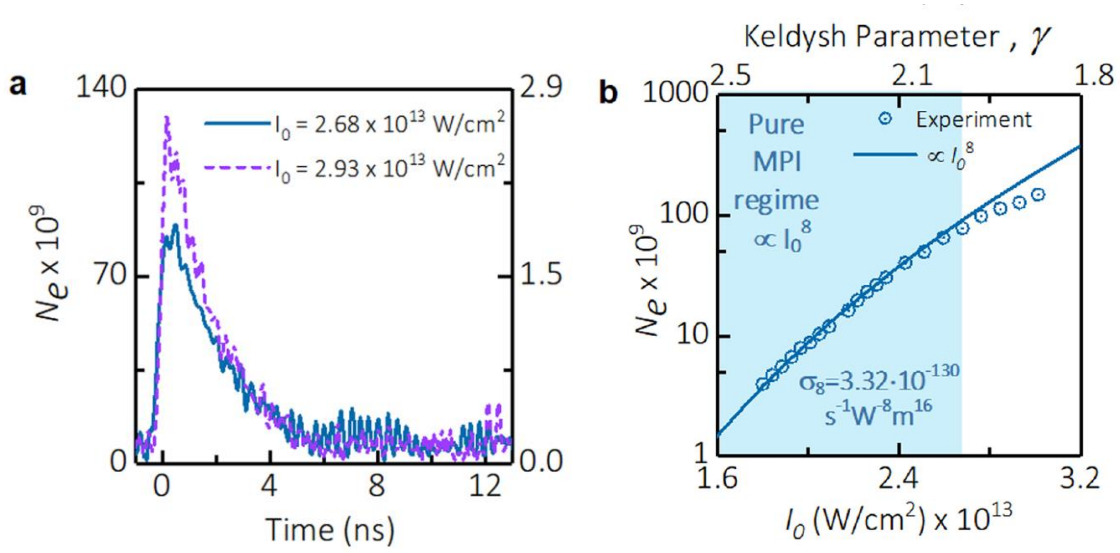


*Figure 11. Absolute measurements of parameters of MPI of air. (a) Temporal evolution of microwave signal scattered from the plasma and total number of electrons in plasma volume Ne(t). (b) Measured dependence of $N_e$ immediately after the plasma creation vs. intensity at the beam center $I_0$. 'Reproduced from* [65] .

## 5. Rotational Temperature Measurements

Radar REMPI has recently been demonstrated to measure rotational temperatures of molecular oxygen and nitrogen in various environments. Rotational REMPI spectra of the molecular species are obtained by scanning the laser wavelengths through multiple rotational lines. The rotational temperatures of the molecular species can be determined from the spectra and analysis of the rotational state distribution, including Boltzmann analysis of rotational states, whole rotational spectrum fitting, and empirical analysis of linewidth fitting, FWHM fitting, slope fitting and area fitting.[37, 38, 40, 66] Compared to single-shot techniques of CARS (Coherent Anti-stokes Raman scattering), Radar REMPI requires measurements at multiple wavelengths by laser scanning or multiple lasers to obtain rotational spectrum. The advantage is that it only requires single-port optical access and can be used for the "see-through-the-wall" temperature measurements.[38] 2+1 REMPI of molecular oxygen has been studied extensively. And similar study on 2+2 REMPI of molecular nitrogen has been studied as well. [67]

The REMPI structure of $O_2(C^3\Pi)$ can be summarized as the following. The ground state, $O_2(X^3\Sigma)$, can be best described as Hund's case (b), in which the projected component of orbital angular momentum on the molecular axis is $\Lambda' = 0$, the projected component of the spin on the molecular axis, $\Sigma'$, can take the values -1, 0, 1 and the projected total angular momentum on the molecular axis, $\Omega'$, is not defined.[68] The splitting due to $\Sigma' = -1$, 0, and 1 leads to the hyperfine structure in the ground state, which has been denoted as $F_1$, $F_2$ and $F_3$, respectively. The excited state of $O_2$ used in this study, $O_2(C^3\Pi)$ can be best described as Hund's case (a), in which $\Lambda = 1$ and $\Sigma$ can take -1, 0, 1, which correspond to $\Omega$ taking the values 0, 1, 2 respectively. The $\Omega$ values lead to the hyperfine structure in the C state, which has been denoted as $S_1$, $S_2$ and $S_3$, respectively.

The 2-photon REMPI spectra obtained in the experiments are convolutions of the hyperfine structures of the molecular oxygen, thermal Doppler and the laser broadening.

The excited state energies of $O_2(C^3\Pi_g(v'=2, J'))$ are fitted by least squares to the polynomials as follows:

$$F_1 = n_{01} + B_{eff1}J'(J'+1) - D_{v1}J'^2(J'+1)^2,$$

$$F_2 = n_{02} + B_{eff2}J'(J'+1) - D_{v2}J'^2(J'+1)^2,$$

$$F_3 = n_{03} + B_{eff3}J'(J'+1) - D_{v3}J'^2(J'+1)^2,$$

where the derived constants are listed in Table 3 based on the previous experimental and computational study of the REMPI spectra of $O_2$.[69-72]

Table 3. Adopted constants for $O_2(C^3\Pi_g(v'=2))$

| $cm^{-1}$ | $F_1$ | $F_2$ | $F_3$ |
|---|---|---|---|
| $n_0$ | 69369 | 69449 | 69552 |
| $B_{eff}$ | 1.630 | 1.653 | 1.691 |
| $D_v$ | $1.9 \times 10^{-5}$ | $1.6 \times 10^{-5}$ | $1.9 \times 10^{-5}$ |

In the two-photon transition $(3s\sigma)C^3\Pi_g \leftarrow\leftarrow X^3\Sigma_g^-$, since the $^3\Pi$ and $^3\Sigma$ states approaches case (a) and case (b), respectively, the band structure is more complicated than other transitions

(i.e. $^2\Pi \leftarrow ^2\Sigma$). Three sub-bands are expected as $^3\Pi_0 \leftarrow ^3\Sigma^-$, $^3\Pi_1 \leftarrow ^3\Sigma^-$, and $^3\Pi_2 \leftarrow ^3\Sigma^-$. In each sub-band there are nine branches, three for each triplet component of the lower state. Thus there are in all 27 branches.[73] In addition, the O, P, Q, R, and S branches are expected according to the selection rule ($\Delta J=0, \pm1, \pm2$). For instance, in an S branch ($\Delta J=+2$), a two-photon transition from ground state $G_1$ to intermediate state $F_3$ giving rise to $S_{31}$. The two photon transition line strength $S^2_{f,g}$ between the excited state $C^3\Pi$, Hund's case (a), and the ground state $X^3\Sigma$, case (b), has been modeled by[74]

$$T^2_{f,g} = \sum_{k=0,2} \frac{\left|\beta_k^{(2)}\right|^2}{2k+1}(2J+1)(2J'+1)(2N'+1)\begin{bmatrix} J' & S & N' \\ \Lambda'+\Sigma & -\Sigma & -\Lambda' \end{bmatrix}^2 \begin{bmatrix} J & k & J' \\ \Omega & -\Delta\Lambda & -\Lambda'-\Sigma \end{bmatrix}^2 \quad (24)$$

where $[...]$ is the Wigner 3-j symbol, $J$ is the rotational quantum number, $N$ is total angular momentum except the spin, $\beta_k^{(2)}$ is the polarization coefficient, and primed parameters denote the ground $X^3\Sigma$ state while unprimed parameters denote the excited $C^3\Pi$ state. For linearly polarized light, terms of both $k$=0 and 2 contribute to the final line strength, $\beta_k^{(2)} = \sqrt{10/3}$, while for circularly polarized light, only k=2 contributes, giving $\beta_k^{(2)} = \sqrt{5}$.

The microwave scattering signal from the REMPI produced plasma is proportional to the total number of electrons inside the plasma[7], which is proportional to the total number of transitions to the continuum through the resonant two photon transition followed by the single photon ionization. The total number of transitions to the continuum is thus determined by the product of the number of molecules in the ground state and the rate of multiphoton ionization. An expression for the resulting microwave scattering signal can be written as [43]

$$E_{MW} \propto N_e = N_0 \cdot T^2_{f,g} I^2 \cdot S_{fi} I \cdot exp\left(-E_g/k_B T\right) \quad (25)$$

where $E_{MW}$ is the scattering microwave electric field, $N_e$ is total electron number inside the plasma generated by REMPI, $N_0$ is the total number of oxygen molecules in the laser focal region, $E_g$ is the energy of the ground state of $X^3\Sigma$, $k_B$ is Boltzmann constant, $T$ is temperature, $I$ is the intensity of the laser beam, and $S_{fi}$ is the ionization cross section from the excited state to the ionization continuum. It should be noted that the rotational quantum number dependence of (2J+1) for the Boltzmann factor cancels in the Equation (16), accounting for the rotational degeneracy of ground state J levels.

The variation of the intensity of the rotational lines in an electronic manifold is determined by the thermal population distribution of the rotational levels. The rotational temperature can be extracted from the analysis of the rotational structures revealed in the REMPI spectra. The thermal distribution of the rotational levels is given by a statistically weighted (i.e. quantum degenerated) Boltzmann factor of $(2J+1)\exp(-E_g/k_BT)$, where the rotational level with the maximum population shifts toward higher $J$ values with increasing temperature. If $S_{fi}$ is assumed to be constant due to limited scanning range and the ground state population $N_0$ is constant during the scan time, then the Boltzmann plots can be formulated as

$$\frac{log\left(\frac{E_{MW}}{I^3 T_{f,g}^{(2)}}\right)}{E_g} \propto -\frac{1}{k_B T} \quad . \qquad (26)$$

When a region of the spectrum including numerous rotational lines is measured, a statistical fit of the Boltzmann plot gives an accurate representation of the rotational populations and thus the rotational temperature, i.e., the slope of the Boltzmann plot as shown in the *Equation (26)*.

The $S_{21}$ branch was chosen for these analyses due to the distinctness in spectral position and intensity among the experimentally observable lines at relatively low temperature (<700K). The calculated rotational line strengths of selected $S_{21}$ branch transitions are shown in Table 4, as an example. Table 4 shows detailed information of the individual transitions, including transition wavelength, the J' rotational level of the ground state, the $G_1$ term energy of that ground state rotational level, and the corresponding $T^{(2)}_{f,g}$ rotational line strength, which is used in the calculation of $O_2$ rotational temperature in Section III.

*Table 4. Selected rotational lines of $S_{21}$ for low temperature measurements*

| Wavelength (nm) | J' | $G_1$ ($cm^{-1}$) | $T^{(2)}_{f,g}$ |
|---|---|---|---|
| 286.09 | 25 | 933.38 | 14.73 |
| 286.24 | 23 | 793.08 | 13.73 |
| 286.38 | 21 | 664.15 | 12.73 |
| 286.52 | 19 | 546.62 | 11.72 |
| 286.65 | 17 | 440.49 | 10.72 |
| 286.78 | 15 | 345.79 | 9.72 |
| 286.88 | 13 | 262.54 | 8.71 |
| 286.99 | 11 | 190.74 | 7.70 |
| 287.09 | 9 | 130.42 | 6.69 |
| 287.18 | 7 | 81.57 | 5.66 |
| 287.26 | 5 | 44.20 | 4.62 |
| 287.34 | 3 | 18.33 | 3.50 |

[40]

At elevated temperature, the S branch lines become congested due to the overlap of multiple branches, including O and P branches, between 286 nm and 287.5nm. A further shift in the population distribution toward higher rotational states due to increased temperature results in a different set of spectral peaks that is distinguishable between 285nm and 286.5nm which is utilized for the elevated temperature extraction. The REMPI rotational lines used for temperature measurements greater than 700 K in the hydrogen/air flame are shown in Table 5. Based on the

known standard temperature of the flames in the Hencken burner, rotational lines with maximum sensitivity within that temperature range were chosen.

*Table 5. Selected rotational lines for elevated temperature measurements*

| Branch | Wavelength (nm) | J' | $G_{\Omega+1}$ ($cm^{-1}$) | $T^{(2)}_{f,g}$ |
|---|---|---|---|---|
| $R_{32}$ | 285.36 | 41 | 2462.02 | 10.456 |
| $P_{31}$ | 285.37 | 48 | 3216.95 | 18.976 |
| $O_{12}$ | 286.05 | 39 | 2231.73 | 14.970 |
| $Q_{32}$ | 286.20 | 37 | 2012.57 | 18.740 |
| $P_{32}$ | 286.34 | 27 | 1085.03 | 9.630 |
| $O_{12}$ | 286.35 | 35 | 1804.59 | 17.740 |
| $Q_{31}$ | 286.45 | 26 | 931.19 | 13.754 |
| $P_{32}$ | 286.58 | 39 | 2231.73 | 20.5 |
| $P_{21}$ | 286.60 | 32 | 1420.03 | 20.247 |
| $Q_{12}$ | 286.62 | 29 | 1248.00 | 12.371 |

By selecting various rotational line peaks in the (2+1) $O_2$ REMPI spectrum, the rotational temperature can be determined by the Boltzmann plot, as shown in Figure 12.

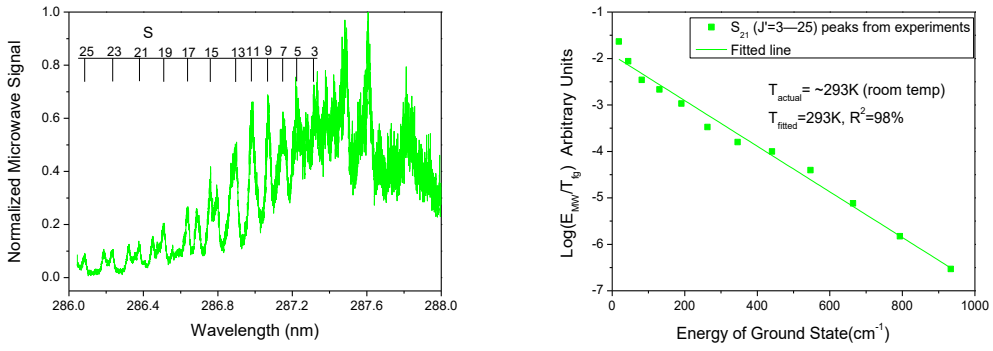


*Figure 12. (a) REMPI spectrum of molecular oxygen in room air, (b) temperature determination by the Boltzmann plot. 'Reproduced from .*

Additionally, whole spectral fitting technique has been conducted for the rotational temperature measurements. The experimental results of the $O_2$ rotational temperature measurements based on the $O_2$ REMPI spectral model are shown in Fig. 13 from subplot (a) to (h). In each plot, the black line is the averaged spectral result from four spectra obtained in the different conditions mentioned above. The red line is the $O_2$ REMPI spectrum simulation result. The experimental temperature and calculated rotational temperature of $O_2$ are both labeled in the figure. Eight different temperatures have been measured in the quartz cell and flame environments. The temperature range is from 294K to 1273K in the quartz cell limited by the heating capability of the furnace. Two flame conditions were demonstrated with higher temperature values i.e., 1610 K in $CH_4$/air flame and 1658 K in $H_2$/air flame. The error of rotational temperature measurement of $O_2$ is less than ±10% with the calculation uncertainty less than ± 50 K with the temperature range of 294 K to 1658 K.

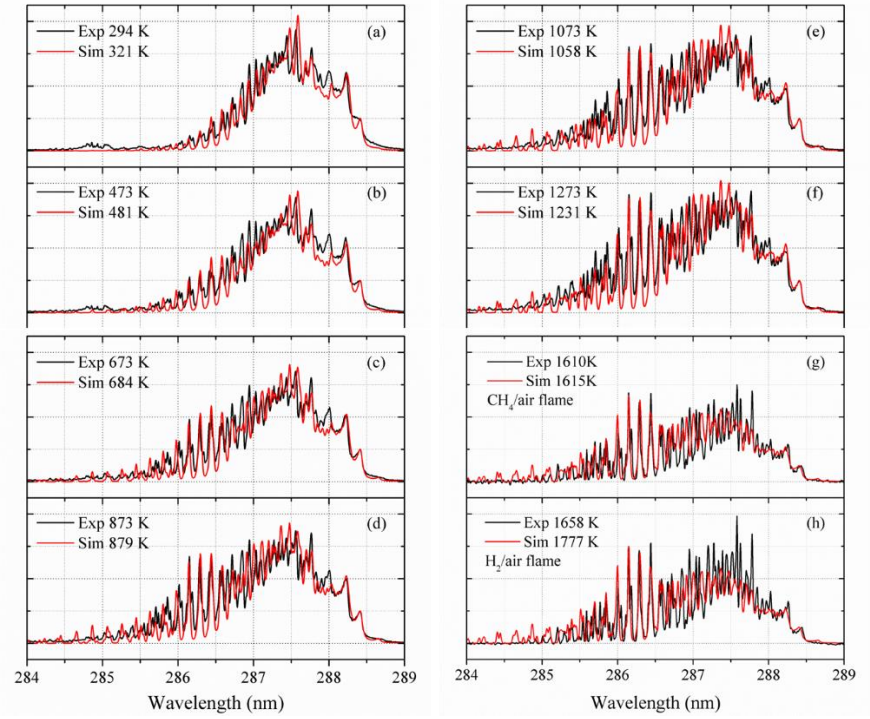

*Figure 13. whole spectra fitting of 2+1 REMPI of molecular oxygen. The conditions are from 294K to 1273K in the heated quartz cell. Two flame conditions were demonstrated with higher temperature values i.e., 1610 K in CH4/air flame and 1658 K in H2/air flame. 'Reproduced from [75].*

Empirical fitting of molecular oxygen has been conducted by linewidth fitting, FWHM fitting, slope fitting and area fitting. The linewidth fitting method was applied in temperature measurements of O2 and ambient air at 1 atm. The values of full width at half maximum (FWHM) were calculated for several spectral peaks within the smoothed O2 rotational spectra. In contrast to linewidth fitting, thousands of data points were used in the linear fitting to extract the temperature from O2 spectra. The right side (34800 cm-1 – 35200 cm-1) of the spectrum shown in Fig. 13, representing higher energy transitions, with S branches dominating the spectral shape, was involved to extract the data slope information highly related to the O2 rotational temperature. Within the normalized spectral profile, the data selection threshold was set at 30%-80% of the peak values with the spectra smoothed over 100 to 1000 points. The area fitting was applied to measure the temperature, not only in O2 and ambient air at low temperature range, but also in H2/air and CH4/air flames with higher temperature values. Due to the unique structure of the REMPI spectrum in molecular oxygen, the area fitting method has been demonstrated to be a viable technique for the remote temperature measurement over a wide temperature range and in dramatically different environments.

## 6. Standoff Detection of Trace Species

Radar REMPI is originally developed as a method for standoff detection of Improvised explosive device (IED). Besides IED detection, standoff detection is required when sampling and sample preparation is not possible, or when sampling takes too much time or poses too great a risk.

In many of these cases the trace species of interest is localized, so long path integrated approaches are not viable.

Detection in the microwave region has numerous advantages over optical detection. Using homodyne or heterodyne technology, the electric field rather than the power can be detected, so much better noise rejection can be achieved and the signal strength falls inversely with distance rather than with distance squared. The long wavelength of the microwaves leads to effective point coherent scattering from the plasma in the laser focal volume, so phase matching is unimportant and scattering in the backward direction is strong. Many microwave photons can be scattered from a single electron, so the amplitude of the scattering can be increased by increasing the power of the microwave transmitter. The low energy of the microwave photons corresponds to thousands of more photons per unit energy than in the visible region, so shot noise is drastically reduced. For weak ionization characteristic of trace species diagnostics, the measured electric field is a linear function of the number of electrons, which is directly proportional to the trace species concentration. Furthermore, there is very little solar or other natural background radiation in the microwave spectral region.

Ten-meter scale standoff detection of NO has been demonstrated with a linear response down to the parts in $10^9$ NO levels in dry air and in laboratory air with 50% humidity. The laser with up to 1mJ of 100 ps pulses at 226nm was focused from 10m away to a beam waist of about 60 μm, corresponding to a focal length of 5 cm. 1+1 REMPI of nitric oxide via $A^2\Sigma^+ \leftarrow X\Pi^2$ manifold was generated in air. The 10mW microwave transmitter with a microwave lens was was placed 1m away from the target. The Radar REMPI signal can be detected in either the backward direction or the parallel direction.

## 7. Summary and Outlook

Since the introduction of the Radar REMPI concept, significant advances have been achieved to understand the physics and mechanism and apply the technique into a wide range of applications in the last decade. The major focus in the past decade was on:

i. Physical understanding of interactions between REMPI and other laser-induced plasmas and microwave
ii. Quantitative characterizations of plasmas, including direct MPI plasma, REMPI plasma, nanosecond/picosecond/femtosecond laser-induced plasmas, atmospheric pressure plasma jets, etc.
iii. Quantitative measurements of species concentrations in reactive and non-reactive environments
iv. Rotational temperature measurements of oxygen and nitrogen in flames and plasmas.
v. Standoff detection of trace species in air.

In this paper, various aspects of Radar REMPI were reviewed, such as advances in fabrication, design, operation and analysis of homogeneous, catalytic, homogeneous-heterogeneous, and excess enthalpy microburners. An overarching theme that emerges from this review is that Radar REMPI has great potentials for diagnostics in reactive and non-reactive flows and plasmas. Important directions of future research of Radar REMPI are likely to occur on several fronts:

1. A new particle in cell modeling of the REMPI plasma might be helpful to understand the plasma kinetics

2. Microwave measurements of ultrafast laser-induced plasmas, especially on the ultrafast dynamics of the plasmas where there are not many diagnostic tools available.

3. Terahertz microwave and electronics are becoming more available, which might drive the Radar REMPI measurements into next level since the detection limit is proportional to the microwave frequency.
4. Combining multiple lasers for Radar REMPI will allow to access the optical transitions in complex molecular species, such as Double Resonance Spectroscopy and optical Rydberg Spectroscopy.
5. Since microwave can penetrate ceramic materials, Radar REMPI only requires minimal optical access. It might be used for diagnostics in challenging environments.
6. Standoff detection as a challenging task might see more applications of Radar REMPI.

**Acknowledgements**

ZZ acknowledges the support by NSF 1418848 and 2026242 and DOE DE-SC0021382. M.N.S. acknowledges partial support by the Princeton Collaborative Research Facility (PCRF)supported by the US DOE under contract DE-AC02-09CH11466. R. B. M acknowledges the support by AFOSR, ONR, and DARPA.

## References


1. Z. Zhang, M.N. Shneider, and R.B. Miles, *Microwave diagnostics of laser-induced avalanche ionization in air.* Journal of Applied Physics, 2006. **100**(7): p. 6.
2. M.N.R. Ashfold and C.M. Western, *Multiphoton Spectroscopy, Applications*, in *Encyclopedia of Spectroscopy and Spectrometry*, J.C. Lindon, Editor. 1999, Elsevier: Oxford. p. 1424-1433.
3. L. Keldysh, *Ionization in the field of a strong electromagnetic wave.* Sov. Phys. JETP, 1965. **20**(5): p. 1307-1314.
4. M.N. Shneider and R.B. Miles, *Microwave diagnostics of small plasma objects.* Journal of Applied physics, 2005. **98**(3): p. 033301.
5. H. Park, C. Chang, B. Deng, C. Domier, A. Donné, K. Kawahata, C. Liang, X. Liang, H. Lu, and N. Luhmann Jr, *Recent advancements in microwave imaging plasma diagnostics.* Review of scientific instruments, 2003. **74**(10): p. 4239-4262.
6. M.A. Heald and C.B. Wharton, *Plasma Diagnostics with Microwaves*. 1965: Wiley.
7. Z. Zhang, *Coherent Microwave Scattering of Laser-induced Plasma*, in *Mechanical and Aerospace Engineering*. 2008, Princeton University: Princeton.
8. J.D. Huba, *NRL plasma formulary*. Vol. 6790. 1998: Naval Research Laboratory.
9. D.M. Pozar, *Microwave Engineering, 4th Edition*. 2011: Wiley.
10. C.A. Galea, M.N. Shneider, M. Gragston, and Z. Zhang, *Coherent microwave scattering from xenon resonance-enhanced multiphoton ionization-initiated plasma in air.* Journal of Applied Physics, 2020. **127**(5): p. 053301.
11. S. McGuire, A. Dogariu, T. Chng, and R.B. Miles. *Methods for enhancing radar REMPI sensitivity*. in *53rd AIAA Aerospace Sciences Meeting*. 2015.
12. A. Dogariu, M.N. Shneider, and R.B. Miles, *Versatile radar measurement of the electron loss rate in air.* Applied Physics Letters, 2013. **103**(22): p. 224102.
13. Y. Wu, J.C. Sawyer, L. Su, and Z. Zhang, *Quantitative measurement of electron number in nanosecond and picosecond laser-induced air breakdown.* Journal of Applied Physics, 2016. **119**(17): p. 173303.
14. A. Shashurin, M. Shneider, A. Dogariu, R. Miles, and M. Keidar, *Temporary-resolved measurement of electron density in small atmospheric plasmas.* Applied Physics Letters, 2010. **96**(17): p. 171502.

15. T. Streibel and R. Zimmermann, *Resonance-enhanced multiphoton ionization mass spectrometry (REMPI-MS): Applications for process analysis.* Annual Review of Analytical Chemistry, 2014. **7**: p. 361-381.
16. F. Rudakov, Y. Gao, X. Cheng, and P.M. Weber, *Non-intrusive detection of combustion intermediates by photoionization via Rydberg states and microwave backscattering.* Combustion and Flame, 2016. **171**: p. 162-167.
17. J.A. Smith, *Laser diagnostics of a diamond depositing chemical vapour deposition gas-phase environment*. 2002, University of Bristol.
18. A.J. van den Brom, M. Kapelios, T.N. Kitsopoulos, N.H. Nahler, B. Cronin, and M.N. Ashfold, *Photodissociation and photoionization of pyrrole following the multiphoton excitation at 243 and 364.7 nm.* Physical Chemistry Chemical Physics, 2005. **7**(5): p. 892-899.
19. M.S. Chou, K. Putman, and R.F. Porter, *Multiphoton ionization of atomic hydrogen in methane pyrolysis.* The Journal of Physical Chemistry, 1986. **90**(26): p. 6805-6807.
20. D. Baulch, J. Griffiths, and R. Richter, *The application of resonance enhanced multiphoton ionization to the detection of hydrogen atoms during the oscillatory combustion of hydrogen.* Proceedings of the Royal Society of London. Series A: Mathematical and Physical Sciences, 1991. **434**(1891): p. 399-412.
21. F. Celii and J. Butler, *Hydrogen atom detection in the filament‐assisted diamond deposition environment.* Applied physics letters, 1989. **54**(11): p. 1031-1033.
22. Y. Gontier, N. Rahman, and M. Trahin, *Resonant multiphoton ionization of atomic hydrogen.* Physical Review A, 1988. **37**(12): p. 4694.
23. S. Dixit, D. Levin, and B. McKoy, *Resonant enhanced multiphoton ionization studies in atomic oxygen.* Physical Review A, 1988. **37**(11): p. 4220.
24. A. Dogariu, J. Michael, E. Stockman, and R. Miles. *Atomic oxygen detection using radar REMPI*. in *Conference on Lasers and Electro-Optics*. 2009. Optical Society of America.
25. M. Gragston, J. Sawyer, S.F. Adams, Y. Wu, and Z. Zhang, *Radar resonance-enhanced multiphoton ionization for measurement of atomic oxygen in non-equilibrium pulsed plasmas.* Journal of Applied Physics, 2019. **125**(20): p. 203301.

26. E. De Beer, C. De Lange, and N. Westwood, *Resonance-enhanced multiphoton-ionization photoelectron spectroscopy of np and nf Rydberg states of atomic nitrogen.* Physical Review A, 1992. **46**(9): p. 5653.
27. A. Fujii and N. Morita, *Detection of nitrogen atoms produced by predissociation of superexcited Rydberg states of NO.* Chemical physics letters, 1991. **182**(3-4): p. 304-309.
28. A. Clark, K. Ledingham, A. Marshall, and R. Singhal, *Resonant ionization spectroscopy of carbon atoms following laser-induced fragmentation of nitro-aromatic molecules.* Spectrochimica Acta Part B: Atomic Spectroscopy, 1992. **47**(6): p. 799-808.
29. S.T. Pratt, J.L. Dehmer, and P.M. Dehmer, *Photoelectron angular distributions from resonant multiphoton ionization of atomic carbon.* The Journal of chemical physics, 1985. **82**(2): p. 676-680.
30. Z. Zhang and M.N. Shneider, *Measurement of plasma decay processes in mixture of sodium and argon by coherent microwave scattering.* Physics of Plasmas, 2010. **17**(3): p. 033108.
31. Y. Wu, J. Sawyer, Z. Zhang, M.N. Shneider, and A.A. Viggiano, *Measurement of sodium-argon cluster ion recombination by coherent microwave scattering.* Applied Physics Letters, 2012. **100**(11): p. 114108.
32. Z. Zhang, M.N. Shneider, and R.B. Miles, *Coherent Microwave Rayleigh Scattering from Resonance-Enhanced Multiphoton Ionization in Argon.* Physical Review Letters, 2007. **98**(26): p. 265005.
33. Y. Wu, Z. Zhang, T.M. Ombrello, and V.R. Katta, *Quantitative Radar REMPI measurements of methyl radicals in flames at atmospheric pressure.* Applied Physics B, 2013. **111**(3): p. 391-397.
34. M. Vrakking, A. Bracker, T. Suzuki, and Y.T. Lee, *Ultrasensitive Detection of Hydrogen Molecules by (2+ 1)[REMPI] Ultrasensitive Detection of Hydrogen Molecules by (2+ 1) REMPI {Resonance-Enhanced Multiphoton Ionization.* Review of Scientific Instruments, 1992. **64**(3).
35. I. Candan, *Production and measurement of H2 in rovibrationally excited states*. 2016, UCL (University College London).

36. A.E. Pomerantz, F. Ausfelder, R.N. Zare, and W.M. Huo, *Line strength factors for E, F1 Σ+ g (v′ = 0, J′ = J′′) X1 Σ+ g (v′′, J′′)(2+ 1) REMPI transitions in molecular hydrogen.* Canadian journal of chemistry, 2004. **82**(6): p. 723-729.

37. Y. Wu, M. Gragston, and Z. Zhang, *Acoustic detection of resonance-enhanced multiphoton ionization for spatially resolved temperature measurement.* Optics Letters, 2017. **42**(17): p. 3415-3418.

38. Y. Wu, M. Gragston, Z. Zhang, and J.D. Miller, *Spatially localized, see-through-wall temperature measurements in a flow reactor using radar REMPI.* Optics Letters, 2017. **42**(1): p. 53-56.

39. Y. Wu, Z. Zhang, and T.M. Ombrello, *Spatially resolved measurement of singlet delta oxygen by radar resonance-enhanced multiphoton ionization.* Optics Letters, 2013. **38**(13): p. 2286-2288.

40. Y. Wu, Z. Zhang, and S.F. Adams, *O2 rotational temperature measurements by coherent microwave scattering from REMPI.* Chemical Physics Letters, 2011. **513**(4): p. 191-194.

41. A. Dogariu and R.B. Miles, *Detecting localized trace species in air using radar resonance-enhanced multi-photon ionization.* Applied optics, 2011. **50**(4): p. A68-A73.

42. Z. Zhang, S. Zaidi, C. Brennan, A. Dogariu, M. Shneider, and R. Miles, *Radar REMPI Detection of NO2 by NO Photo-Fragments*, in *47th AIAA Aerospace Sciences Meeting including The New Horizons Forum and Aerospace Exposition*. 2009, American Institute of Aeronautics and Astronautics.

43. Z. Zhang, M.N. Shneider, S. Zaidi, and R.B. Miles, *Temperature Measurement of Nitric Oxide by RADAR REMPI.* 46th AIAA Aerospace Sciences Meeting and Exhibit, 2008.

44. P.J.H. Tjossem, P.M. Goodwin, and T.A. Cool, *Two‐photon resonance REMPI detection of the formyl radical.* The Journal of Chemical Physics, 1986. **84**(10): p. 5334-5343.

45. J.S. Bernstein, X.-m. Song, and T.A. Cool, *Detection of the formyl radical in a methane/oxygen flame by resonance ionization.* Chemical Physics Letters, 1988. **145**(3): p. 188-192.

46. Y. Wu, A. Bottom, Z. Zhang, T.M. Ombrello, and V.R. Katta, *Direct measurement of methyl radicals in a methane/air flame at atmospheric pressure by radar REMPI.* Optics Express, 2011. **19**(24): p. 23997-24004.

47. L. Su, *Laser diagnostics of C2H4 and CH4 from n-butane pyrolysis.* 2016.
48. N.M. Khambatta, L.J. Radziemski, and S.N. Dixit, *Upper bound for a three-photon excitation cross section in atomic argon in the ultraviolet regime.* Physical Review A, 1989. **39**(8): p. 3842-3845.
49. J. Bokor, J. Zavelovich, and C.K. Rhodes, *Multiphoton ultraviolet spectroscopy of some $6p$ levels in krypton.* Physical Review A, 1980. **21**(5): p. 1453-1459.
50. A.M. Mebel and S.-H. Lin, *Excited electronic states of the methyl radical. Ab initio molecular orbital study of geometries, excitation energies and vibronic spectra.* Chemical physics, 1997. **215**(3): p. 329-341.
51. A.M. Velasco, I. Martin, and C. Lavín, *Rydberg electron transitions in the methyl radical.* Chemical Physics Letters, 1997. **264**(6): p. 579-583.
52. M.A. Childs, K.L. Menningen, L.W. Anderson, and J.E. Lawler, *Oscillator strengths of CH3 in the vacuum ultraviolet.* Chemical Physics Letters, 1995. **246**(6): p. 567-570.
53. M.J. Pilling, A.M. Bass, and W. Braun, *Oscillator strengths of CH2 and CH3 in the vacuum ultraviolet.* Chemical Physics Letters, 1971. **9**(2): p. 147-148.
54. J. Zhou, J.J. Lin, W. Shiu, S.-C. Pu, and K. Liu, *Crossed-beam scattering of F + CD[sub 4] --> DF + CD[sub 3](nu NK): The integral cross sections.* The Journal of Chemical Physics, 2003. **119**(5): p. 2538-2544.
55. M.N. Shneider, Z. Zhang, and R.B. Miles, *Plasma induced by resonance enhanced multiphoton ionization in inert gas.* Journal of Applied Physics, 2007. **102**(12): p. 123103.
56. M.N. Shneider, Z. Zhang, and R.B. Miles, *Simultaneous resonant enhanced multiphoton ionization and electron avalanche ionization in gas mixtures.* Journal of Applied Physics, 2008. **104**(2): p. 023302.
57. I.S. Grigoriev and E.Z. Meæilikhov, *Handbook of physical quantities*. 1997.
58. M. Kogan, *Rarefied gas dynamics Plenum Press New York.* 1969.
59. M.N. Shneider and R.B. Miles, *Laser induced avalanche ionization in gases or gas mixtures with resonantly enhanced multiphoton ionization or femtosecond laser pulse pre-ionization.* Physics of Plasmas, 2012. **19**(8): p. 083508.
60. Y.P. Raizer and J.E. Allen, *Gas discharge physics*. Vol. 2. 1997: Springer Berlin.

61. Y. Wu, Z. Zhang, N. Jiang, S. Roy, and J.R. Gord, *Resonant- and avalanche-ionization amplification of laser-induced plasma in air*. Journal of Applied Physics, 2014. **116**(14): p. 143304.

62. Z. Zhang, *Quantitative Microplasma Electron Number Density Measurement by Coherent Microwave Rayleigh Scattering.* IEEE Transactions on Plasma Science, 2011. **39**(1): p. 593-595.

63. X. Wang, P. Stockett, R. Jagannath, S. Bane, and A. Shashurin, *Time-resolved measurements of electron density in nanosecond pulsed plasmas using microwave scattering.* Plasma Sources Science and Technology, 2018. **27**(7): p. 07LT02.

64. X. Wang, A. Patel, and A. Shashurin, *Combined microwave and laser Rayleigh scattering diagnostics for pin-to-pin nanosecond discharges.* Journal of Applied Physics, 2021. **129**(18): p. 183302.

65. A. Sharma, M.N. Slipchenko, M.N. Shneider, X. Wang, K.A. Rahman, and A. Shashurin, *Counting the electrons in a multiphoton ionization by elastic scattering of microwaves.* Scientific Reports, 2018. **8**(1): p. 2874.

66. S.F. Adams, Y. Wu, and Z. Zhang, *Oxygen Rotational Temperature Determination Using Empirical Analyses of C3 $\Pi(v' = 2) \leftarrow X3 \Sigma(v'' = 0)$ Transitions.* Applied Spectroscopy, 2015. **69**(9): p. 1036-1041.

67. S. McGuire and R. Miles, *Collision induced ultraviolet structure in nitrogen radar REMPI spectra.* The Journal of Chemical Physics, 2014. **141**(24): p. 244301.

68. G. Herzberg, *Molecular Spectra and Molecular Structure: Spectra of Diatomic Molecules* 2nd ed. 1989, New York: Krieger Pub Co.

69. B.R. Lewis, S.T. Gibson, J.S. Morrill, and M.L. Ginter, *Perturbations in the 3s sigma(g) (1,3)Pi(g) Rydberg states of O-2: Bound-bound interactions with the second (1)Pi(g) and (1)Delta(g) valence states.* Journal of Chemical Physics, 1999. **111**(1): p. 186-197.

70. J. Sawyer, Y. Wu, Z.L. Zhang, and S.F. Adams, *O-2 rotational temperature measurements in an atmospheric air microdischarge by radar resonance-enhanced multiphoton ionization.* Journal of Applied Physics, 2013. **113**(23).

71. Y. Wu, J. Sawyer, Z.L. Zhang, and S.F. Adams, *Flame temperature measurements by radar resonance-enhanced multiphoton ionization of molecular oxygen.* Applied Optics, 2012. **51**(28): p. 6864-6869.

72. Y. Wu, Z.L. Zhang, and S.F. Adams, *O-2 rotational temperature measurements by coherent microwave scattering from REMPI.* Chemical Physics Letters, 2011. **513**(4-6): p. 191-194.

73. G. Herzberg, *Molecular Spectra and Molecular Structure. Volume I: Spectra of Diatomic Molecules.* 2nd ed. 1950: D. Van Nostrand.

74. C. Mainos, *Multiphoton rotational line strength in diatomic molecules and for states with Hund's case-(a) or case-(b) coupling.* Physical Review A, 1986. **33**(6): p. 3983.

75. Y. Wu, Z. Zhang, and S.F. Adams, *Temperature sensitivity of molecular oxygen resonant-enhanced multiphoton ionization spectra involving the C3Πgintermediate state.* Applied Physics B, 2016. **122**(5): p. 149.